Journal of Hydrology 681 (2026) 136676

Contents lists available at ScienceDirect

Journal of Hydrology

journal homepage: www.elsevier.com/locate/jhydrol

Climate change induced hydrological regime shifts in the transboundary Zarafshon River Basin in Central Asia

Sonu Khanal [a,b], Philip Kraaijenbrink [c], Faezeh Nick [c], Joel Fiddes [d], Arthur Lutz [a], Evan Miles [e,f], Esteban Garcia [g], Brecht Haeyer [b], Johannes Hunink [b], Walter Immerzeel [c,*]

[a] Hydrominds, Utrecht, the Netherlands
[b] FutureWater, Wageningen, the Netherlands
[c] Utrecht University, Department of Physical Geography, Utrecht, the Netherlands
[d] WSL Institute for Snow and Avalanche Research SLF, Davos, Switzerland
[e] Laboratory of Hydraulics, Hydrology, and Glaciology (VAW), ETH Zürich, Zürich, Switzerland
[f] Swiss Federal Institute for Forest, Snow, and Landscape Research (WSL), bâtiment ALPOLE, Sion, Switzerland
[g] Deutsche Gesellschaft für Internationale Zusammenarbeit GmbH, Tajikistan

ARTICLE INFO

This manuscript was handled by Ryan T. Bailey, Editor-in-Chief

Keywords:
Hydrological shifts
Climate change impacts
Central Asia
Snowmelt
Glacier melt
Transboundary River

ABSTRACT

Mountain river basins in Central Asia are highly sensitive to climate-driven changes in snow and glacier melt, yet the magnitude and timing of the resulting hydrological regime shifts remain poorly quantified. To address this gap, we assess present and future hydrological shifts in the transboundary Zarafshon River Basin with the SPHY glacio-hydrological model. We improved the representation of snowmelt and snow infiltration, which re-distributes water to delayed baseflow and improves winter and spring discharge. We calibrated the improved model against discharge observations, satellite-derived snow cover and glacier mass balance data through Monte Carlo optimization.

Over 1991–2020, snowmelt dominates runoff (52.4%), followed by baseflow (23.3%) and rainfall-runoff (21.1%), whereas glacier melt contributes 3.2% but sustains late-summer low flows. Snow and glacier melt dominate the upstream hydrology, whereas rainfall-runoff and baseflow sustain the flow in the lower basin. Using downscaled ISIMIP3b climate scenarios, we project glacier volume to decline by ~ 40% under SSP126 and ~ 80% under SSP585 by 2100. Annual total runoff declines by less than 7% in all scenarios, because gains in rainfall-runoff and baseflow almost offset the melt loss. Peak total runoff declines by 22.6% under SSP585, and the annual peak discharge shifts earlier by 22–38 days. The hydrological regime shift from snowmelt to rainfall-runoff is more pronounced in the Fondarya than in the Matcha River system.

These results indicate a shift from a snowmelt to a rainfall-runoff dominated hydrological regime. Such a shift would reduce summer water availability and increase irrigation stress, highlighting the need for adaptive management.

1. Introduction

The majority of water resources in Central Asia (CA) originate from 'water towers', with high-altitude mountain ranges such as the Pamirs and the Tien Shan playing a crucial role in sustaining river flow and downstream demands (Chen et al., 2016; Huss and Hock, 2018; Olsson et al., 2010; Sorg et al., 2012). Glaciers in CA cover about 17,000 km^2, more than 60% of which lies in Tajikistan (Gafforzoda et al., 2023). Water generated in the mountains plays a crucial role in the socioeconomic development of CA and, in particular, Tajikistan relies on irrigation for more than 90% of its agricultural production, which sustains over half of its workforce (World Bank, 2024). Tajikistan has been experiencing increased vulnerability to climate-induced changes, threatening its agricultural, economic, and environmental systems (Reyer et al., 2017). Adaptation to climate change is urgently needed to sustain livelihoods and safeguard the water resources underpinning economic development in Tajikistan and Uzbekistan.

The Zarafshon River Basin (ZRB) in Tajikistan was historically a tributary of the Amu Darya but under current conditions the river generally no longer reaches the main stem (Karimov et al., 2022; UNEP,

* Corresponding author at: Vening Meineszgebouw A, Princetonlaan 8a, 3584 CB Utrecht, the Netherlands.
E-mail address: W.W.Immerzeel@uu.nl (W. Immerzeel).

https://doi.org/10.1016/j.jhydrol.2026.136676
Received 9 March 2026; Received in revised form 30 September 2026; Accepted 23 October 2026
Available online 28 October 2026
0022-1694/© 2026 The Author(s). Published by Elsevier B.V. This is an open access article under the CC BY license (http://creativecommons.org/licenses/by/4.0/).

2011). Even so, ZRB waters remain vital for economies and communities in Tajikistan and downstream oases in Uzbekistan. Agriculture is the dominant water user in the Zarafshon system, particularly in Samarkand, Bukhara and Karshi, where it sustains ~ 1.1 million ha of irrigated land, linking basin hydrology directly to irrigation reliability and food security. The Zarafshon River delivers 5.1–5.3 km^3 yr^{-1} at the Tajik-Uzbek border, of which roughly 5.1 km^3 yr^{-1} is allocated to irrigation through the Ravatkhodja headworks (design capacity 1350 m^3 s^{-1}) and multiple downstream storage and diversion structures (Khaidarov, 2020). However, the water generated within the catchment is insufficient to meet this high irrigation demand. As a result, 60% (8.3 billion cubic meters) of the total water used for irrigation is pumped from the Amu Darya (Ragettli et al., 2025). The seasonality of river flow in the ZRB is largely driven by meltwater from snow and glaciers, causing distinct seasonal peaks in river discharge. During the spring and summer months, snowmelt contributes substantially to the river's flow, while glacier melt provides a more continuous source of water that peaks later in the year, typically during the late summer or early autumn. The ZRB, a hotspot for climate change impacts, has experienced significant glacier mass loss in recent decades. Historical observations indicate a steady decline in glacier extent, with projections suggesting accelerated retreat under future warming scenarios (IPCC, 2022). Furthermore, rising temperatures disrupt snow accumulation and melt cycles during the spring and early summer, leading to earlier peak flows and reduced late-season water availability (Huss and Hock, 2018). These climate-driven changes pose a significant threat to upstream and downstream water security by altering glacier and snowmelt dynamics and consequently affecting the hydrological cycle (Farinotti et al., 2015; Kraaijenbrink et al., 2017). Changes in the cryosphere also strongly influence the frequency and intensity of natural hazards (Ding et al., 2020; Harrison et al., 2018; Veh et al., 2020). These challenges are further compounded by the complex transboundary nature of water resources in the region, where numerous countries share water systems, further complicating cooperative management efforts (Micklin, 2016; O'Hara, 2000).

While previous studies have assessed glacier mass balance changes in the region (Barandun et al., 2021, 2020), fewer have explicitly quantified the implications of changes in the flow components (snowmelt, rainfall and groundwater) and downstream water availability (Pohl et al., 2017). The quantification of the flow components is crucial for adaptive water resource planning, as shifts in meltwater seasonality and magnitude directly affect irrigation, hydropower, and ecosystem services (Immerzeel et al., 2020). As the cryosphere continues to decline with further warming, there is a growing need to quantify the specific roles that melt and the other flow contributors play in timing and magnitude of water availability (Kang et al., 2010; Kraaijenbrink et al., 2017). Glacio-hydrological models (GHMs) are invaluable tools for addressing these challenges (Immerzeel, 2010). However, the application of these GHMs in the high mountains of CA is hindered by sparse and fragmented in-situ observations and limited data exchange across agencies and borders (Pepin et al., 2015). The use of remotely sensed data alongside limited in-situ observations helps to address the problem of data scarcity in simulating water availability with GHMs (Huang et al., 2026). A GHM that can incorporate available remote sensing data with limited in-situ observations is needed to effectively assess long-term climate change impacts on cryospheric and hydrological processes across scales in CA.

Currently in SPHY GHM, snowmelt is simulated by applying a degree-day factor to the positive part of the daily mean air temperature, and the meltwater leaving the snowpack is routed directly to the channel as quick runoff, bypassing the unsaturated zone (Terink et al., 2015). Both assumptions are poorly met in high altitude catchments. The first leads to underestimates of melt on days with a sub-zero mean air temperature but a positive maximum air temperature, common through the cold seasons and at high elevation (Hock, 2003). The second, excludes meltwater from infiltrating to the soil, and hence from being available for evapotranspiration and delayed release, removing the subsurface memory by which spring melt sustains late-season flow (Huang et al., 2026). We address both by integrating melt over a diurnal temperature cycle and infiltrating a calibrated fraction of meltwater into the root zone for release as delayed subsurface runoff and baseflow. Neither modification is novel in terms of process physics; the contribution lies in quantifying their impact. Resolving sub-daily melt and allowing meltwater to infiltrate improves the simulated hydrograph specifically in winter and spring, the seasons the original formulation reproduces worst, by shifting water from direct snowmelt runoff to delayed baseflow and postponing the spring rising limb. Neither process is represented in the standard snow routine used in previous SPHY applications across the high mountains of Asia and CA (Khanal et al., 2021; Lutz et al., 2014; Wijngaard et al., 2017).

This study addresses these gaps by quantifying historical and future snow and glacier melt contributions to river discharge in the ZRB, providing critical insights for sustainable water management in a warming climate. First, we improve the representation of snow processes in GHM to better represent snowmelt simulation and snow infiltration. Second, we simulate hydrological processes in the ZRB for the historical period using a state-of-the-art GHM, distinguishing the flow components (glacier melt, snowmelt, baseflow and rainfall-runoff). Third, we assess the impacts of climate change on the individual flow components and their seasonality during the 21st century. Finally, we investigate future changes in total water availability and peak-runoff at different spatial and temporal scales. This research contributes to the ongoing efforts to adapt to climate change and safeguard water resources, with the aim of supporting science-based policies to ensure water security for the ZRB's agricultural sector, economic development, and overall climate resilience.

2. Study area

The Zarafshon River, once a critical tributary of the Amu Darya, originates from the Zarafshon Glacier at 2775 m in the western Pamir-Alay (Fig. 1). With an average discharge of 158 m^3 s^{-1} at Panjakent, it supports 0.5 million ha of irrigated agriculture and sustains water demands for over six million people in Tajikistan and Uzbekistan (Abdushukurov et al., 2022). From its source (i.e. Zarafshon glacier), the river flows westward with a gradient of 5.1% over a distance of 260 km, traversing a canyon-like valley carved by two mountain ranges, forming the upper reach known as the Matcha River (Groll et al., 2013). On the southern left bank, flowing between the Turkestan and Zarafshon ranges, it joins with the Yagnob and Mogiyon rivers, as well as many small tributaries (Abdushukurov et al., 2022). Near Ayni, it merges with the Fondarya River, originating from the south, and becomes known as the Zarafshon River. After traveling 170 km, the river enters Uzbekistan downstream of Panjakent, reaching the lowlands of the Aral Sea basin. Passing through a flat region and crossing the Tajikistan-Uzbekistan border, it flows through Samarkand and Bukhara before vanishing in the desert near Karakul.

The ZRB covers 12,276 km^2 in Tajikistan, with elevations ranging from about 5500 m at the headwater to about 875 m where the river leaves Tajikistan. The basin contains 849 glaciers covering 532.9 km^2; the largest, Zarafshon Glacier, is 27.8 km long and 87.2 km^2 in area (RGI Consortium, 2017). Glacier elevations range from ~ 2775 to ~ 5400 m, with a mean elevation of ~ 4100 m (Fig. 1b). Since 1930 the glacierized area of Tajikistan has shrunk by about 30% and the ZRB follows a similar trend (Sultonov and Pant, 2026). The Zarafshon Glacier terminus retreated by about 1.7 km between 1979 and 2019, and glacier area in the upper ZRB declined at a rate of 0.015 km^2 yr^{-1} between 2010 and 2019 (Halimov et al., 2026).

CA is considered as a transition region for the westerlies and Indian summer monsoon (Murodov et al., 2023). The Pamir, Hindu Kush, Tianshan, and Himalayan mountains to the southeast of CA block most of the moisture from the Indian summer monsoon(Khanal et al., 2023). However, during strong monsoon seasons, the excess moisture can

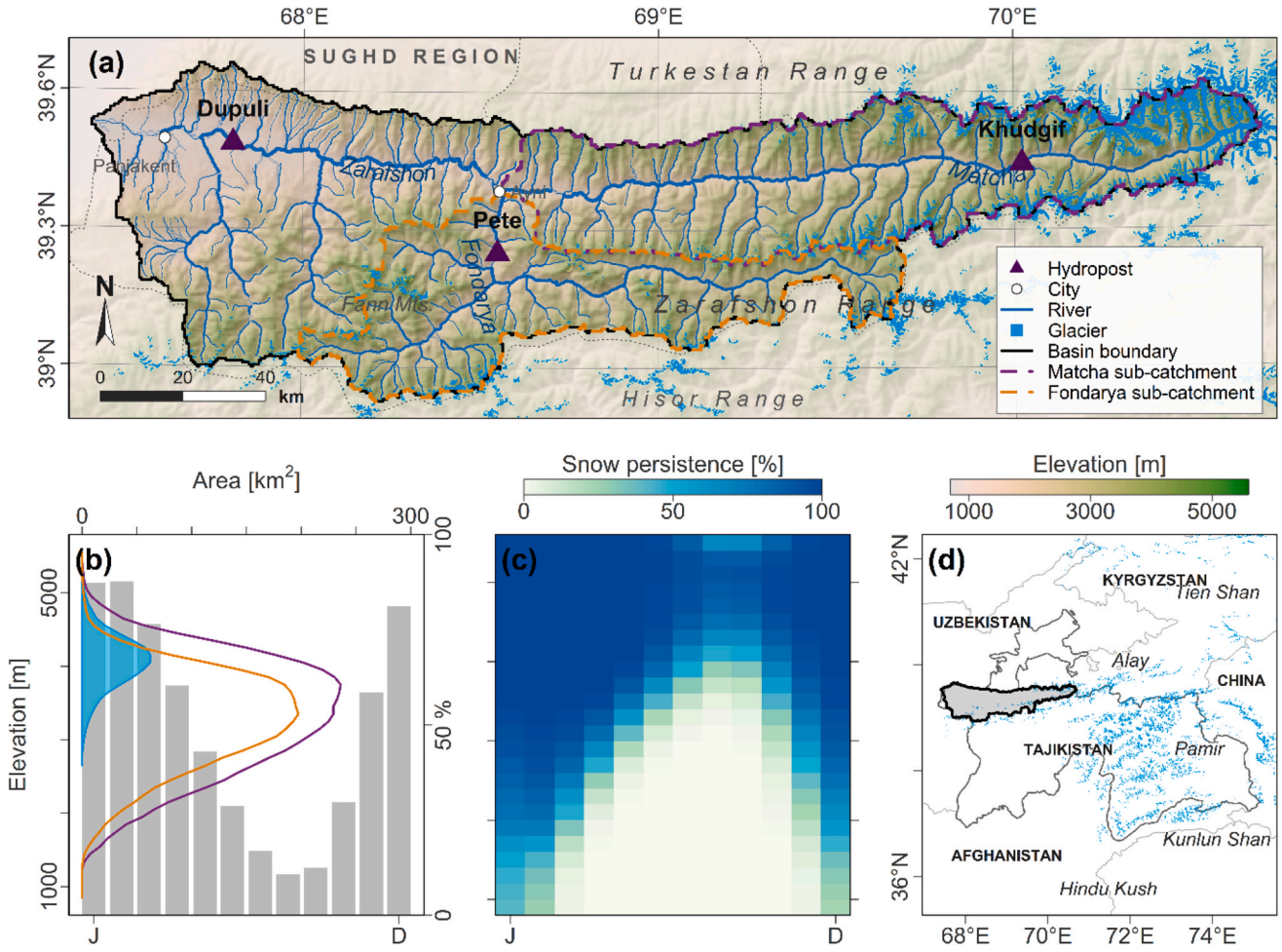


Fig. 1. (a) The Zarafshon River Basin (ZRB), its glaciers and tributaries. Purple triangles are hydroposts (discharge stations) with data available after the year 1991. (b) Hypsometry of the glaciers, Fondarya and Matcha catchments (primary y-axis) and monthly (J-January to D-December) average basin snow persistence (secondary y-axis expressed in %). (c) Snow persistence expressed in % per 100 m elevation bins. (d) Zarafshon basin in the context of Central Asia and other mountain ranges. (For interpretation of the references to colour in this figure legend, the reader is referred to the web version of this article.)

propagate westward, resulting in increased rainfall in southern and southeastern CA (Chen et al., 2021; Nzabarinda et al., 2024). The climate of the ZRB is influenced mostly by arid midlatitude westerlies with negligible influence from the Indian summer monsoon (Lu et al., 2020). Therefore, the ZRB has a continental and arid climate, with strong seasonal and interannual variability (Aalto et al., 2017). Western disturbances bring heavy winter snowfall, with snow persistence exceeding 80% from December to March, and areas above 4000 m remain snow-covered most of the year (Fig. 1b and 2c). Annual precipitation levels are extremely low in the main valley of the basin, ranging from 100 to 400 mm (Savoskul and Smakhtin, 2013). Consequently, livelihoods in these areas depend almost entirely on accessing river water rather than direct rainfall. This reliance highlights the importance of irrigation infrastructure and accurate flow components modeling to assess surface runoff availability across the ZRB (Ragettli et al., 2025).

3. Data and methods

3.1. Glacio-hydrological model

In this study, we use the Spatial Processes in Hydrology (SPHY) v3 model (Khanal et al., 2021), set up at a daily timestep and 500 × 500 m spatial resolution. SPHY is a "leaky-bucket" type water balance model designed for cryospheric–hydrological simulations at glacier, sub-basin, basin, and regional scales. It integrates hydrological processes such as rainfall–runoff, evapotranspiration, soil water dynamics, snow accumulation and melt, glacier accumulation and melt, and glacier evolution (Terink et al., 2015).

For each grid cell, dynamic storages are maintained for snow, soil water, and groundwater. Snowmelt runoff is computed for the snow-covered grid cell over the land surface, with runoff over the glacier surface defined as glacier runoff. A degree-day method, using calibrated melt rates, is implemented to calculate snowmelt (Hock, 2005, 2003). The model also considers the refreezing of meltwater within the snowpack.

Snow infiltration is critical for groundwater recharge in nival–glacial systems, particularly in the Pamir, where winter precipitation is mainly as snow (Huang et al., 2026). However, the SPHY model does not account for snowmelt infiltration into the soil. Therefore, we modify SPHY to include snowmelt infiltration into the soil layer based on saturation-excess principles. By implementing a fraction of snowmelt (i.e. a calibration factor "SnowF" ranging from 0 to 1), daily snowmelt runoff is allowed to infiltrate into the soil's root zone. Physically, SnowF represents the combined effect of the slow meltwater release at the base of a ripe snowpack, the high infiltration capacity of coarse, frozen-but-permeable mountain soils, and the absence of overland-flow pathways under a continuous snow cover. The remaining fraction (1 − SnowF) represents melt on saturated or impermeable ground and preferential flow to the channel network. Infiltrated melt then follows the normal

soil–water routine: it raises root-zone storage, is available for evapotranspiration and, on exceeding field capacity, percolates to the groundwater store from which baseflow is generated. SnowF is treated as a single basin-wide calibration parameter in this study.

We further improved the snowmelt routine compared with the previous SPHY snowmelt module. The existing degree day parameterisation uses mean daily temperature to calculate melt, and therefore it misses melt during days when temperature is above zero for a part of the day, but average temperature is still below zero (Eq. (1):

$$A_{pot,t} = \begin{Bmatrix} T_{avg,t} \bullet DDF_s, if T_{max,t} > 0 \\ 0, if T_{max,t} \leq 0 \end{Bmatrix} \quad (1)$$

Therefore, in the improved simulation, for the days when maximum temperature is above zero, we calculate the fraction of the day where the hourly temperature is above zero, assuming that temperature during the day follows a cosine pattern (Eq. (2) and Eq. (3).

The improved daily potential snowmelt is calculated as:

$$A_{pot,t} = \begin{Bmatrix} HT_t \bullet DDF_s, if T_{max,t} > 0 \\ 0, if T_{max,t} \leq 0 \end{Bmatrix} \quad (2)$$

$$HT_t = \sum_{i=1}^{i=24} \{Max(0, (T_{avg,t} + (T_{max,t} - T_{avg,t})\cos(\pi * i/12))/24)\} \quad (3)$$

Where $T_{avg,t}$ [°C] is the mean air temperature on day t, $A_{pot,t}$ [mm] is the potential snowmelt on day t, $T_{max,t}$ [°C] is the maximum air temperature on day t and DDF_s [mm °C^{-1}d^{-1}] is a calibrated degree day factor for snow. HT_t ℃] is mean above-freezing temperature for the fraction of the day during which the hourly temperature exceeds the melting point. The potential snowmelt is subsequently used to calculate the actual snowmelt, which is limited by the amount of snow available to melt. Once actual snowmelt exceeds the storage capacity, snowmelt runoff is produced.

We set up the glacier module for the ZRB at 50 × 50 m sub-grid resolution. The Randolph Glacier Inventory (RGI Consortium, 2017) is intersected with the 500 x 500 m model resolution to identify the glaciers that lie in each model grid cell. Each glacier part is then assigned a unique-id. Each glacier part is further divided into debris-covered and debris-free parts using the methods from Kraaijenbrink et al. (2017). The initial ice thickness and volume from Farinotti et al. (2019) are then assigned to each glacier part. For each glacier part, the mean elevation from a 50x50 m digital elevation model is calculated (Farr et al., 2007). This is required to lapse daily air temperature from the model grid cell mean elevation to the glacier's mean elevation. Glacier ice accumulation and melt are calculated based on the initial ice volume, daily precipitation and temperature for each glacier part. The degree day factors for debris-covered and debris-free glaciers are used to calculate the melt. Future changes in glaciers are assessed by using a mass conserving ice redistribution approach. The details are explained in Khanal et al. (2021).

The rainfall-runoff is calculated as the sum of surface runoff from rainfall and lateral flow from the soil water storage layer, with surface runoff based on saturation excess. The soil water storage capacity is influenced by soil hydraulic properties, and reference evapotranspiration is calculated using the modified Hargreaves method (Hargreaves and Samani, 1985). Reference evapotranspiration is converted to potential evapotranspiration based on land use type. Actual evapotranspiration is limited by the soil water content at permanent wilting point. When saturation excess occurs, excess water contributes to river discharge through lateral flow or surface runoff. A dynamic groundwater storage in each grid cell contributes to the generation of delayed baseflow runoff. All runoff types are routed downstream using a simple recession coefficient method. For details of the process representation in SPHY, readers are referred to Terink et al. (2015). The overall workflow, from the input data through the model and its calibration to the analyses reported here, is summarized in Fig. 2.

3.2. Data

SPHY requires both static and dynamic input data. Key static inputs include a digital elevation model (DEM), land use, glacier cover and thickness (distinguishing debris-free and debris-covered ice), lakes/reservoirs, and soil properties (Table 1). The main dynamic inputs are climate data, including daily precipitation and daily mean, minimum, and maximum temperatures.

3.2.1. Climate data

The meteorological forcing for SPHY is generated by the topography-based downscaling scheme TopoSCALE (Fiddes and Gruber, 2014). TopoSCALE downscales atmospheric fields available on pressure levels to a high-resolution digital elevation model. In this case, the atmospheric model data are provided by the latest generation of European Centre for Medium-Range Weather Forecasts (ECMWF) reanalysis product, ERA5 (Hersbach et al., 2020).

TopoSCALE performs a 3D interpolation of atmospheric fields available on pressure levels, to account for time-varying lapse rates, and a topographic correction of radiative fluxes. The latter includes a cosine correction of incident direct shortwave radiation on a slope, adjustment of diffuse shortwave and longwave radiation by the sky view factor, and elevation correction of both longwave and direct shortwave radiation. It has been extensively tested in various geographical regions and applications, e.g., permafrost in the European Alps (Fiddes et al., 2015), permafrost in the North Atlantic region (Westermann et al., 2015), Northern hemisphere permafrost (Obu et al., 2019), Antarctic permafrost (Obu et al., 2020), Arctic snow cover (Aalstad et al., 2018), Arctic climate change (Vikhamar Schuler and Østby, 2020) and Alpine snow cover (Fiddes et al., 2019). TopoSCALE can therefore provide hillslope scale model forcing without any requirement for ground data by accounting for the main topographic effects on atmospheric forcing.

The SPHY hydrological model forced with ERA5-TopoSCALE precipitation produced simulated discharge that exceeded observations by 63–108% (PBIAS) at the three gauging stations under default parameter values (Fig. S1d). An error of this magnitude cannot be compensated by parameter calibration(Immerzeel et al., 2015). It indicates a systematic overestimation of precipitation in the mountain catchments, which has been reported for ERA5 precipitation products before (Dahri et al., 2021; Khanal, 2021; Orsolini et al., 2019) (Fig. S2). Comparison with the seven GHCN-Daily stations (Menne et al., 2012) within the basin shows that the ratio of simulated to observed precipitation increases with elevation, from 0.59 at the lowest station to between 1.6 and 3.6 at stations lying between approximately 1,400 and 3,550 m (Fig. S1a, b). We therefore adopted an elevation-dependent correction factor (Fig. S1a). The factor ranges from 0.7 to 3 and increases linearly between 2,000 and 4,000 m. We applied it as a divisor to the daily ERA5-TopoSCALE precipitation fields. Because the correction is constant in time, the temporal variability, the wet-day frequency, and the relative magnitude of extreme events in the forcing are preserved. The magnitude of the correction was constrained hydrologically and the version that produced a PBIAS within ± 10% at all three gauges under default uncalibrated parameters was retained (Moriasi et al., 2007; Fig. S1d), and was then held fixed during the subsequent model calibration. The full derivation, the station records and the alternatives tested are given in Supplementary Text S1.

3.2.2. Snow cover

The 500 m resolution MODIS MOD10A1 (hereafter MODIS) daily snow cover data (2000–2020) is used in this study to calculate monthly snow persistence maps (Hall and Riggs, 2015). Snow persistence here is defined as the fraction of time a pixel is covered with snow (Fig. S3). Average monthly snow persistence maps are used to calibrate relevant model parameters by comparing simulated to observed snow cover.

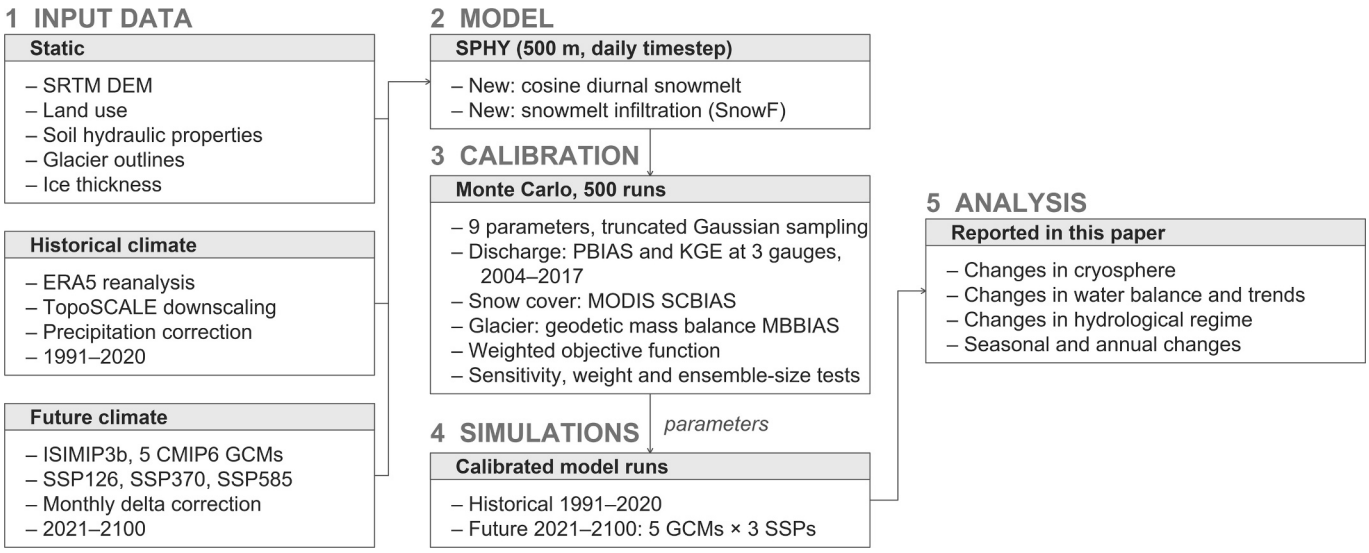


Fig. 2. Schematic of the modelling workflow including the inputs, methods, model and its two structural improvements, simulations and analysis.

Table 1
Overview of static and dynamic input datasets used in the SPHY glacio-hydrological model for the Zarafshon River Basin.

SN	Dataset	Type	Spatial resolution	Temporal resolution	Period	Source
1	ERA5 downscaled data with TopoSCALE –Minimum temperature –Maximum temperature –Mean temperature –Precipitation	Historical climate	0.25°	Daily	1940 – present	Hersbach et al. (2020)Fiddes & Gruber (2014)
2	ISIMIP3b GCM	Future climate projection	0.5°	Daily	2021–2100	Lange (2021)
3	MODIS MOD10A1	Snow cover	500 *m*	Daily	2000 – present	Hall & Riggs (2015)
4	RGI v6.0 glacier outlines	Glacier	–	Static	2017	RGI Consortium (2017)
5	Glacier ice thickness	Glacier	50 *m*	Static	2000	Farinotti et al. (2019)
6	Debris cover mask	Glacier	30 *m*	Static	2000	Kraaijenbrink et al. (2017)
7	Ice surface velocity	Glacier	50 *m*	Static	2017 – 2018	Millan et al. (2022)
8	Geodetic glacier mass balance	Glacier	~100 m elevation bands	Annual	2000 – 2019	Hugonnet et al. (2021)
9	SRTM DEM	Elevation	30 *m*	Static	2000	Farr et al. (2007)
10	ESA CCI	Landcover	300 *m*	Annual	1992 – present	Kirches et al. (2014)
11	HiHydroSoil v2.0	Soil hydraulic properties	250 *m*	Static	2020	Simons et al. (2020)

3.2.3. *Glaciers*

We use altitudinal Surface Mass Balance (SMB) data for four of the major glaciers in the basin (RGI Consortium, 2017) to calibrate and validate the glacier module. These are Zarafshon glacier (Glacier ID 1317829), Rama glacier (Glacier ID 1322248), glacier Rossnich (Glacier ID 1322829), and Shakhisafid glacier (Glacier ID 1322898) (Fig. S4). We use Zarafshon glacier for the calibration and other three glaciers for the independent validation (Fig. S5). Altitudinal SMB is calculated following the method of Miles et al. (2021), solving the continuity equation under the assumption that englacial and basal mass changes are not significant, and that firn densification rates are constant. Ice flux divergence is calculated using ice thickness data (Farinotti et al., 2019) and observed ice surface velocity data from 2016 to 2017 (Millan et al., 2022), then filtered using an ice thickness-dependent spatial filter of the flux divergences (Van Tricht et al., 2021). Surface elevation change measurements are used to derive 2015–2019 SMB across different areas and altitudes, accounting for uncertainties in the data and methods (Hugonnet et al., 2021). Uncertainties are particularly high in the accumulation areas due to limitations in the underlying datasets and the firn (snow older than 1 year) densification assumptions may not fully hold in this domain.

3.2.4. *Discharge*

There are 28 discharge stations in the ZRB; however, most of them have either data available until the 1980 s or are on the tributaries of the main Zarafshon River. The number of stations with discharge data available during the model simulation period is limited. For this study, we selected three stations with the most recent and long-term data record; two in the main Zarafshon River and one in the Fondarya tributary, to calibrate and validate the ZRB SPHY model (Fig. 1 and Table 2). Missing observed discharge values were not gap-filled. We chose the calibration and validation windows, from 2004 till 2017, to maximise the overlap of the three stations, and the number of observed days. The model performance indicators were evaluated only on days with observations, and missing days were excluded from the statistical analysis.

3.2.5. *Other data*

We use the 1 arcsec (~30 m) Shuttle Radar Topography Mission

Table 2
Observed discharge stations in the ZRB-SPHY model domain. The record period of each station is given in the table; model calibration and validation use the common window 2004–2017.

Station	River	Resolution	Start	End	Years	Missing data (%)
Khudgif	Matcha	daily	1991	2010	20	30% (1993–1994, 1996–1999)
Pete	Fondarya	daily	1991	2017	27	4% (1997)
Dupuli	Zarafshon	daily	1991	2017	27	31% (1994, Jan–Feb and Nov–Dec 1996, 1998–2004)

(SRTM) digital elevation model (DEM) data to calculate slope, cell drainage direction, downscale temperature fields, and derive mean glacier elevation for melt calculations (Farr et al., 2007). Hydraulic soil properties are derived from HiHydroSoil (250 m) and resampled to ZRB SPHY model resolution (Simons et al., 2020). Land-use data were obtained from the European Space Agency Climate Change Initiative (ESA CCI, 300 m resolution) dataset (Kirches et al., 2014). All the datasets used in the ZRB SPHY model are resampled to 500 m resolution.

3.3. Model calibration and performance gain with new implementation

3.3.1. Monte Carlo optimization of the parameters

Limited availability of hydro-meteorological data, such as streamflow, precipitation, and snowpack measurements, hinders the accurate representation of hydrological processes in the calibration procedure. Although observed discharge from three stations in the ZRB is available, as well as remotely sensed snow cover extents and glacier mass balances, it remains challenging to validate and fine-tune models in high mountain environments.

To achieve optimal simulations, we generated an ensemble of 500 individual model simulations using a Monte Carlo procedure (Mishra, 2009). In the procedure, each model simulation was run with a randomly sampled parameter set. Nine different model parameters were sampled stochastically from a truncated Gaussian distribution, i.e., a Gaussian distribution with fixed minimum and maximum values (Geweke, 1998). The parameters and their distribution and sampling ranges are presented in Table 3. The means, standard deviations and bounds are based on previous SPHY applications in the region (Huang et al., 2026; Khanal et al., 2021; Lutz et al., 2014; Murodov et al., 2025; Wijngaard et al., 2017).

To assess the performance of each individual simulation within the ensemble of 500 simulations and select the best performing run overall, we used a combination of weighted hydrological and cryospheric evaluation statistics at each discharge station in an objective function per discharge station. This objective function quantifies the difference between observed and simulated data, and by minimizing the function's result, we selected the optimum model parameter set. The functions of the three stations were then combined using weights in a final basin-wide objective function. The runs in the top ten of best performing objective values (i.e. lowest result) were evaluated and the individual run with the most realistic set of parameters from a hydrological perspective was selected as final parameter set for the analysis.

To evaluate the streamflow simulation in the calibration procedure, we use percent bias (PBIAS) and the Kling-Gupta efficiency (KGE) to assess model performance (Nash and Sutcliffe, 1970; Schaefli and Gupta, 2007). These indicate absolute cumulative deviations and how well the timing of peaks in the hydrograph match, respectively. To evaluate the model performance for glacier surface mass balance simulation, we compare the total difference in absolute glacier mass balance (MBBIAS) between the observations and simulations over the entire altitudinal range of Zarafshon Glacier. The performance in the snow cover simulation is evaluated by calculating the sum of normalized climatological snow cover bias (SCBIAS) for the months March–June and between 1,500 and 3,500 m elevation, which is an indicator of simulated snow cover accuracy in the main snowmelt season, being the most relevant period from a hydrological perspective.

An objective value is defined for each station using the following objective function that combines the statistics described above (see Eq. (4). Note that PBIAS, KGE, SCBIAS, and MBBIAS are first scaled from their original range to 0–1:

$$O_s = w_1\text{PBIAS} + w_2(1\text{-KGE}) + w_3\text{SCBIAS} + w_4\text{MBBIAS} \quad (4)$$

Where O_s is the objective value for each individual station and w_n are the weights applied to each of the statistics. We assigned highest weight to the KGE ($w_2 = 1.5$) metric, to put emphasis on streamflow correlation, followed by PBIAS ($w_1 = 0.7$), MBBIAS ($w_4 = 0.5$) and SCBIAS ($w_3 = 0.2$).

Each objective value for a station is subsequently combined to a total objective value (O_{tot}) using station specific weights (w_d, w_p, w_k) using Eq. (5):

$$O_{tot} = w_d O_{\text{Dupuli}} + w_p O_{\text{Pete}} + w_k O_{\text{Khudgif}} \quad (5)$$

Where we assigned highest weight to the catchment of Dupuli station ($w_d = 1.0$), because it is the most downstream and covers a larger part of the basin (10,266, 2,967 and 1,086 km^2 for Dupuli, Pete and Khudgif) compared with the Pete ($w_p = 0.5$) and Khudgif ($w_k = 0.5$) stations.

To test how sensitive the calibration outcome is to these choices, we performed three additional analyses. First, we computed the Spearman rank correlation (ρ) between each sampled parameter and O_s per station and also for O_{tot}. Second, we repeated the ranking of all 500 runs for 2,000 alternative weight sets in which all seven weights in Eqs. (4) and (5) were independently perturbed by up to ± 50%. Third, we tested the adequacy of the ensemble size with bootstrap ensembles of 50 to 500 runs.

Finally, parameter uncertainty in the simulated flow for the reference period was quantified from the ten best-performing parameter sets. The uncertainty spread reported here is the standard deviation across these ten runs computed on the 1991–2020 monthly climatology.

Table 3
Model parameters varied in the Monte Carlo procedure, the characteristics of the truncated normal distribution used for each of them, and final calibrated model parameter values. The parameters were calibrated against observations over 2004–2017.

Parameter	*Description*	*Mean*	*Min*	*Max*	*SD*	*Cal. value*	*Unit*
CapRiseMax	Maximum capillary rise to rootzone	0.5	0	1	0.1	0.571	mm d^{-1}
alphaGw	Baseflow days	0.5	0.1	1	0.2	0.508	
kx	Routing coefficient	0.95	0.85	1	0.05	0.971	–
GlacF	Fraction of glacier melt to baseflow	0.4	0	1	0.2	0.555	–
TCrit	Threshold temperature for snowfall	1	−1	3	1	−0.52	°C
DDFS	Degree day factor for snow	4	1	10	2	1.401	mm °C^{-1} d^{-1}
SnowSC	Snowpack water holding capacity	0.3	0	0.6	0.2	0.196	–
SnowF	Fraction of snowmelt infiltration to soil	0.5	0	1	0.2	0.274	–
Tcorr_fact	Global temperature correction factor	0	−2	2	0.4	−0.485	°C

3.3.2. Performance gain with new implementation

To isolate the effect of the structural modifications, we compared two configurations of the model that are identical in forcing, parameterisation and initial conditions and differ only in structure: (i) the original SPHY formulation, in which potential snowmelt is computed linearly from daily mean air temperature and all snowmelt leaves the cell as direct snow runoff; and (ii) the new implementation, in which the diurnal temperature cycle is resolved by a cosine interpolation, and a fraction SnowF of the snowmelt infiltrates into the soil, from where it reaches the channel as delayed soil runoff and baseflow. Both configurations were run at daily resolution for the short period 2004–2010 to reduce the computational effort; the first year was discarded as spin-up and the evaluation covers 2005–2010. Performance gain was quantified with the NSE of daily discharge at Dupuli, which covers 84% of the ZRB, computed for the full year and separately for the standard seasons (Winter: December to February, Spring: March to May, Summer: June to August and Autumn: September to November).

To test whether the improvement depends on the choice of the new parameter (SnowF), we performed a Monte Carlo experiment of 50 additional runs of the new implementation with SnowF sampled from a truncated Gaussian distribution over its full physical range (0–1), and evaluated each run against the same observations. These additional runs were used to quantify the effect of SnowF on the simulated flow components at Dupuli gauge and to isolate the effect of the structural changes on the model results.

3.4. Future climate projections

Future climate forcing for this study is obtained from the Inter-Sectoral Impact Model Intercomparison Project (ISIMIP), specifically ISIMIP3b (Lange, 2021), which provides bias-corrected climate data from the Coupled Model Intercomparison Project Phase 6 (CMIP6). We use all five CMIP6 general circulation models (GCMs) included in ISIMIP3b (i.e. GFDL-ESM4, IPSL-CM6A-LR, MPI-ESM1-2-HR, MRI-ESM2-0, UKESM1-0-LL), the historical scenario (i.e. 1850–2014), and all three future shared socioeconomic pathway (SSP) scenarios (i.e. 2015–2100; SSP126, SSP370, SSP585). SSP126 represents low emissions with strong mitigation efforts, SSP370 represents moderate emissions with some mitigation, and SSP585 represents high emissions with minimal mitigation (Lange, 2021).

The raw ISIMIP3b data are downscaled using innovative trend-preserving methods to align with W5E5, which shares the same source data as the ERA5-TopoSCALE reference forcing used in this study and consequently has largely similar climatologies and precipitation and temperature distributions. To downscale the ISIMIP3b data to the model resolution, we correct ISIMIP3b for each model grid cell by monthly mean deltas between ERA5-TopoSCALE and the historical scenario of ISIMIP3b over 1991–2014. These deltas are subsequently applied to the future daily ISIMIP3b series (i.e. separately to each combination of model ($n = 5$) and scenario ($n = 3$), so total $n = 15$), using the delta for the associated month of each specific day of the year. Since precipitation in summer is relatively low in the ISIMIP3b ensemble compared with the ERA5-TopoSCALE, high multiplicative delta factors exist for the summer months (Fig. S6). On very rare occasions, when the monthly ERA5 reference precipitation is very small compared with very wet future conditions, the ratio consequently reached values of ten or more. Such high ratios are the numerical artifact rather than a physically plausible change in precipitation, and would generate unrealistic amounts when applied to a wetter month. This may cause single extreme events in the future to be greatly exacerbated to unrealistically high magnitude. We therefore applied a maximum precipitation cutoff to the downscaled daily precipitation series, ensuring that the daily precipitation sums could not exceed the precipitation sum of the ERA5-TopoSCALE reference for a given month by more than a factor 2. Since this study addresses seasonal and annual water availability rather than flood magnitudes, the projections should not be used to infer changes in daily precipitation extremes. In the climate change impact analysis, we assess the differences between the historical reference period (1991–2020) and future time horizons—Mid-Century (MC: 2036–2065) and End-of-Century (EoC: 2071–2100)—across the four seasons: autumn (September–November), winter (December–February), spring (March–May), and summer (June–August).

4. Results

4.1. Historical and future climate

4.1.1. Historical climate

Precipitation amounts vary significantly along the West-East transect in the ZRB (Fig. 3d). The northern and northwestern regions are drier, while the southern and eastern parts are wetter, reflecting the influence of steep topography and orographic effects imposed by the Alay and Tian Shan ranges. Annual precipitation ranges from $\sim$ 500 mm yr^{-1} in the western basin to $\sim$ 1750 mm yr^{-1} in the eastern and southern regions (Fig. 3d). The spring season dominates the seasonal precipitation distribution and contributes 34% of the annual precipitation (Fig. 3c). The basin-aggregated annual precipitation time series (1991–2020) in the ZRB does not show any significant trends (Mann Kendall, hereafter MK, trend, $p > 0.05$).

The ZRB has a high annual variability in annual average temperature ranging from −7.5 to 15.4 °C (Fig. 3b). Monthly temperature shows a distinct seasonal cycle where the temperature is higher for the summer months compared with the winter months (Fig. 3a). The average temperature is highest for July (11.9 °C) and lowest for January (−5.7 °C). The largest variability in the basin-aggregated monthly average temperature is found in the winter months. In contrast to precipitation, the annual average temperature shows a significant (MK trend, $p < 0.05$) increasing trend of 0.035 °C yr^{-1}.

4.1.2. Future climate

The projected changes in the annual basin-averaged temperature and precipitation, comparing the EoC with the reference period, are shown in Fig. 3e and Fig. 3f. All the climate models predict that the future will be warmer compared with the reference period, while the signals for precipitation change are mixed (Fig. 3e). For example, the MPI-ESM1-2-HR model and the GFDL-ESM4 model under SSP370 both project a decrease in precipitation by about 3% and 5%, respectively, by the EoC. In contrast, the UKESM1-0-LL model projects that, under the SSP585 scenario, temperatures will rise by approximately 7.2 °C while precipitation is expected to increase by $\sim$ 23%.

Temperature increases are projected for every month, though the magnitude varies seasonally, with summer likely warming more strongly than other months (Fig. S6). In contrast, changes in precipitation are less uniform. Winter season may see precipitation increases while summer could experience decreases.

4.2. Model calibration

4.2.1. Multi-objective model calibration

Final calibrated parameters from the Monte Carlo procedure and objective function minimization are listed in Table 3. Calibration of the SMB gradient in the ZRB resulted in an optimal setting of both the DDFG and DDFDG parameters to 4 mm $°C^{-1}$ d^{-1}. Both DDFG and DDFDG were fixed before the Monte Carlo procedure and are therefore not among the nine parameters listed in Table 3. Published field-based studies on degree-day factors for debris-covered ice span more than an order of magnitude; 11.1 and 5.3 mm $°C^{-1}$ d^{-1} under 10 mm and 400 mm of debris for Khumbu Glacier in Nepal (Kayastha et al., 2000), 8.0 mm $°C^{-1}$ d^{-1} under 2 mm dusted ice in Dokriani Glacier in Indian Himalayas (Singh et al., 2000), 5.5–6.8 mm $°C^{-1}$ d^{-1} and 1.3–2.5 mm $°C^{-1}$ d^{-1} under 5 mm and 400 mm of debris in Karakoram (Muhammad et al., 2020) and 7.73 mm $°C^{-1}$ d^{-1} and 1.13 mm $°C^{-1}$ d^{-1} under 10 mm and 400 mm

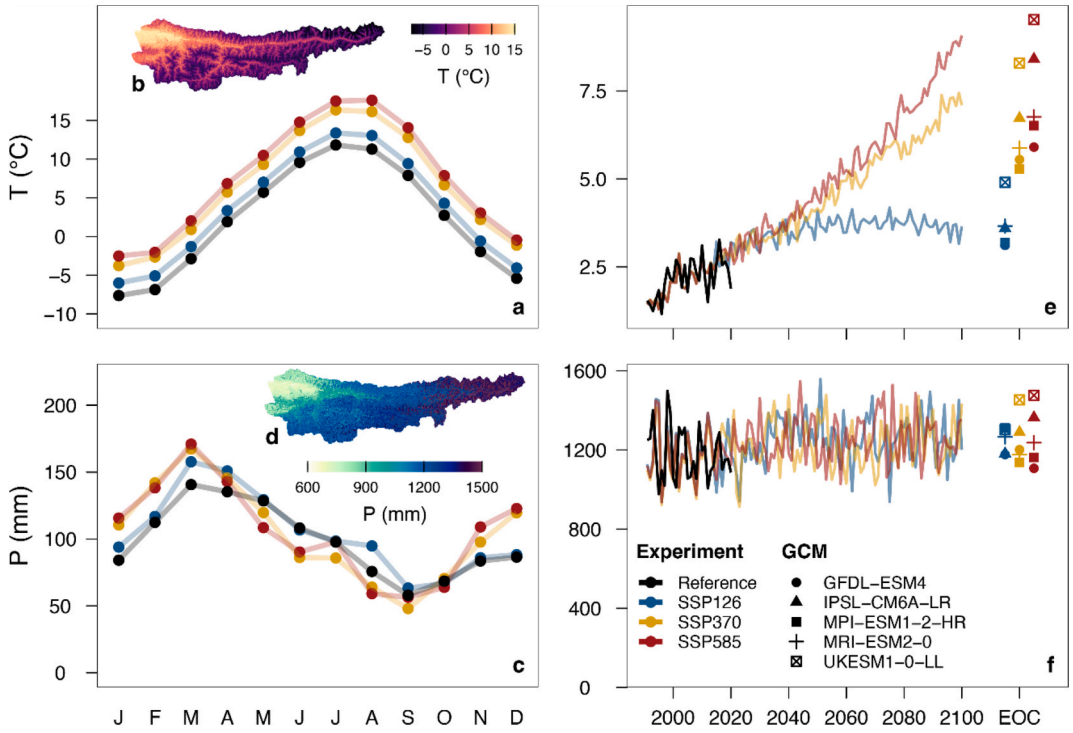


Fig. 3. Historical (1991–2020) and projected (2021–2100) temperature and precipitation of the Zarafshon River Basin. Basin-average monthly mean climatological temperature (a) and precipitation (c) for the reference period (1991–2020) from ERA5-TopoSCALE and end-of-century (EoC, 2071–2100) from ISIMIP3b SSP ensemble means. Spatial distribution (b, d) of mean annual temperature and precipitation of the ERA5-TopoSCALE reference (1991–2020). Basin-average annual mean temperature (e) and precipitation (f) of the ERA5-TopoSCALE reference and ISIMIP3b SSP ensemble mean future projections. The points denote the EoC (2071–2100) mean temperature (e) and precipitation (f) of each GCM within the SSP ensembles.

debris thickness for Baltoro glacier in Karakoram (Mihalcea et al., 2006). Further, a recent model intercomparison suggests that these parameters are strongly site-specific and cannot be transferred between glaciers without local calibration data (Pellicciotti et al., 2026). In the absence of debris thickness or thermal property measurements for the glaciers of the ZRB, a separately calibrated DDFDG would have remained an unconstrained free parameter. We therefore adopted a single effective factor of 4 mm, which sits in the middle of the reported field-based range and is constrained by the altitudinal surface mass balance profiles of the four monitored glaciers. Nevertheless, the calibrated glacier SMB shows good agreement with observed values and generally falls within the uncertainty range of the measurements (Fig. S5). The model reproduces the observed altitudinal SMB gradient in the upper ablation zones and captures the inversion in debris-covered areas (Bisset et al., 2020). The overall mass balance is in good agreement with the observed values.

Monthly modeled snow cover aligns well with MODIS data, though snow cover is slightly overestimated at mid-elevations (>3,500 m) during the actual melt season, i.e., March–June (Fig. S7). Reproducing the observed runoff at the streamflow gauges required more simulated snowmelt, which in turn underestimates snow cover above 3,500 m during June–August. Given the total amount of snow in the ZRB and the temperature index model parameterization, the biases are small. This discrepancy is likely due to limitations inherent in the model structure, as the temperature-index approach and the simple binary snow cover representation struggle to capture the small-scale spatial variability and complex melt dynamics of the thinner snowpacks common at low to mid elevations.

Discharge simulations at the three gauging stations (Dupuli, Pete and Khudgif) show good agreement between observations and model simulations (Fig. 4 and Table 4), as indicated by the high Nash-Sutcliffe efficiency criterion (NSE), coefficient of determination (R^2), and the Kling-Gupta efficiency (KGE), and the low overall percent bias (PBIAS). Only the PBIAS for Khudgif is relatively high at −19.4% which can be attributed to larger biases in year 2004, 2006 and 2010. These larger biases are most likely caused by inaccuracies in the ERA5-TopoSCALE precipitation forcing for this catchment and partly due to SPHY not fully resolving the high altitude processes such as permafrost, sublimation, avalanches, etc. Most peaks in the hydrographs of the different stations are accurately represented. Since for most stations the performance is satisfactory, we consider the calibrated model suitable to assess climate change impacts.

4.2.2. *Sensitivity of the model parameters and weights*

The sensitivity analysis (Fig. S8) shows that model performance is mostly controlled by the snow degree-day factor DDFS (Spearman $\rho = 0.64$), the temperature correction Tcorr_fact ($\rho = 0.33$) and the snowpack water holding capacity SnowSC ($\rho = -0.27$). The glacier melt fraction GlacF ($\rho = -0.53$) and the routing coefficient kx ($\rho = 0.44$) matter only at the glacierized Khudgif headwater, where glacier melt contributes a large share of the flow and flow peaks are erratic; downstream at Pete and Dupuli their effect is small. The remaining parameters show a weak relation with performance ($\rho < 0.16$). The top ten runs are distributed across a wide range of sampled values, therefore the observations do not point to one best value for them — the well-known equifinality problem (Beven, 2001; Pellicciotti et al., 2012).

Of the 500 simulations, run 380 (second-lowest objective value) was selected as the final calibrated parameter set in preference to the top-ranked run 420, which performed worse at Dupuli, a gauge draining 84% of the basin (Fig. 5). The final model selection outcome is insensitive to moderate changes in the weights of Eqs. (4) and (5): under 2000 random perturbations of all seven weights by ± 50%, the rank-1 run keeps rank 1 in 99.6% of the weight sets, the selected run stays at rank 2–3 in 80% and within the top 10 in 95% of them (Fig. 5a). Furthermore, the ten best runs fall well inside the sampled ranges of all parameters, which shows the bounds in Table 3 did not constrain the result (Fig. 5b). For all nine parameters the thick blue line is short and lies on the original

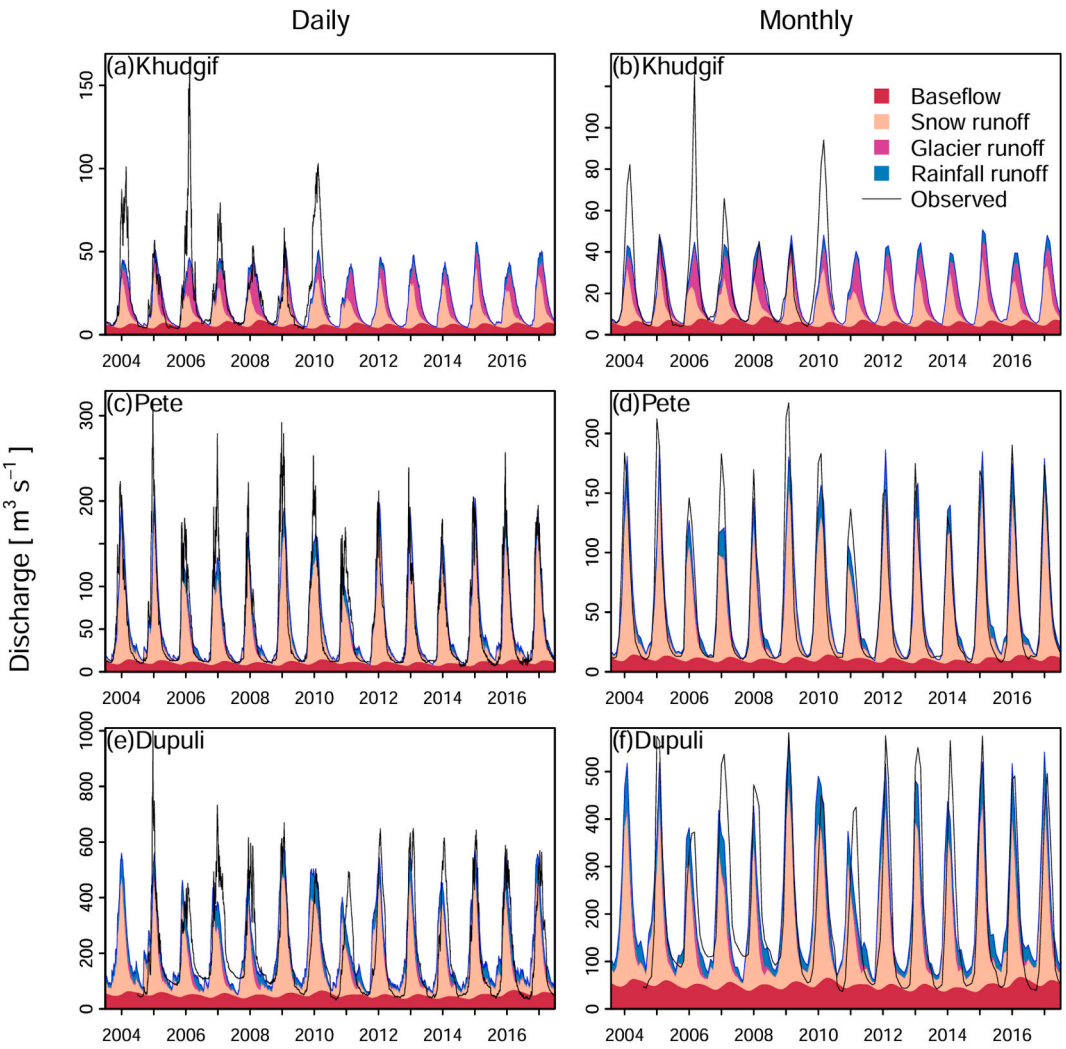


Fig. 4. Observed and simulated discharge with the distinction of flow components (baseflow, snow, glacier and rain runoff) at three calibration and validation stations (hydropost) locations: Khudgif (a, b), Pete (c, d) and Dupuli (e, f), for 2004–2017.

Table 4
Goodness-of-fit statistics of simulated versus observed discharge at daily and monthly time scales, and mean relative contributions of runoff components (B:baseflow, S: snowmelt runoff, G: glacier melt runoff, and R: rainfall-runoff) to total streamflow at the three gauging stations (Khudgif, Pete, and Dupuli) in the Zarafshon River basin over the calibration period 2004–2017. Model performance is evaluated using the percent bias (PBIAS, %), Nash–Sutcliffe efficiency (NSE), coefficient of determination (R^2), and Kling–Gupta efficiency (KGE).

	Daily				Monthly				Contribution (%)			
Station	PBIAS	NSE	R^2	KGE	PBIAS	NSE	R^2	KGE	B	S	G	R
Khudgif	−19.43	0.58	0.69	0.49	−19.34	0.60	0.71	0.50	28.60	38.80	23.3	9.30
Pete	2.00	0.85	0.86	0.84	1.94	0.88	0.89	0.86	18.50	62.90	2.30	16.30
Dupuli	3.32	0.7	0.76	0.76	3.45	0.72	0.72	0.77	23.60	53.10	3.70	19.60

median, so the parameter values identified by the calibration hardly change when the weights change.

Ensemble size adequacy was evaluated using bootstrap ensembles of 50 to 500 runs drawn with replacement from the 500 Monte Carlo simulations (Fig. S9a). For ensembles of 150 runs or more, 95% of the bootstrap samples contained at least one parameter set with top ten performance, and the width of the 90% sampling interval of the sensitivity indices (Fig. S9b) decreased from 0.54 for n = 50 to 0.16 for n = 500 without altering the ranking of the most influential parameters. These results indicate that 500 simulations are sufficient to delineate the region of well-performing parameter sets and to identify the parameters that control model performance.

The ten best-performing runs, selected on their fit to the 2004–2017 observations of discharge, snow cover and glacier mass balance, provide a measure of the parameter uncertainty of the simulated runoff composition. Across these ten runs the mean annual discharge at the outlet over 1991–2020 spans 240 to 258 $m^3\ s^{-1}$, a range of 7.4%. The partitioning of that discharge is less well constrained. Expressed as the mean of the ten runs ± 1 standard deviation, snowmelt runoff contributes 53.4 ± 11.5%, baseflow 22.8 ± 5.8%, rainfall-runoff 21.2 ± 5.7% and glacier melt runoff 2.5 ± 1.6% of total runoff over the same period. These ensemble means differ slightly from the contributions of the selected parameter set reported below, and the spread is carried forward as ± 1 standard deviation on the reference total runoff in the seasonal

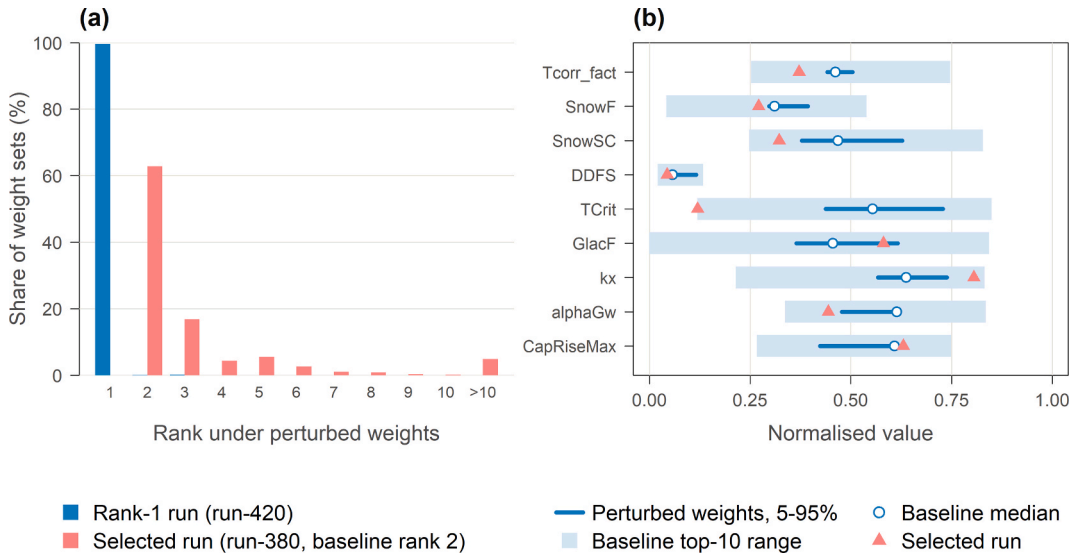


Fig. 5. Robustness of the Monte Carlo calibration outcome to the objective function weights tested by perturbing all seven weights of Eqs. (4) and (5) independently by up to ± 50%. (a) Distribution of the rank attained by the baseline rank-1 run (run 420) and by the selected run (run 380, baseline rank 2) when all seven weights are perturbed. (b) Parameter values of the ten best-performing runs, normalized to each parameter's sampled range. The shading spans the baseline top-10 runs and the open circle marks their median, the thick blue line spans the 5–95% range of the top-10 median across the 2000 perturbed weight sets, and the triangle marks the selected run. All objective values are computed over the 2004–2017 calibration period. (For interpretation of the references to colour in this figure legend, the reader is referred to the web version of this article.)

regime figures of Section 4.4.3. Five GCMs were propagated through the full calibrated model chain for each SSP and therefore represent the input uncertainty for the future projections. However, the parameter ensemble, the top 10 runs, was not propagated through the climate projections, and structural uncertainty and uncertainty in the historical meteorological forcing were not quantified.

4.2.3. Model performance gain with new implementation

The effect of the structural modifications on model performance was quantified by running the original and the modified structure over 2004–2010, using 2004 as spin-up (Fig. 6). At Dupuli, the NSE of daily discharge over the full evaluation period increased from 0.68 to 0.72. The seasonal evaluation shows that this gain originates almost entirely from the cold season and the onset of the melt season, with NSE increasing by 0.45 in winter and 0.62 in spring, and reflects the intended function of SnowF. The infiltrated meltwater recharges the root zone and the groundwater store, raising the simulated baseflow contribution to total flow from 10% to 18%, while the direct snowmelt contribution decreases from 75% to 57% (Fig. S10); the enhanced baseflow sustains winter discharge and delays the spring rising limb, which the original structure simulated too early and too high. Part of the redistributed melt reappears in the rainfall-runoff component, which in SPHY comprises all lateral root-zone outflow irrespective of the origin of the water. Autumn improved marginally (+0.04), and summer remained unchanged because discharge is then dominated by glacier melt, which bypasses the soil column and is insensitive to SnowF. Overall discharge decreased by less than 8% over the full parameter range, the reduction resulting from additional evapotranspiration from the wetter root zone, so the modifications redistribute water among flow paths while leaving the basin water balance essentially closed.

The dependence of the result on the choice of SnowF was examined with 50 Monte Carlo runs (Fig. 6b). Because the infiltrated flux is proportional to SnowF, baseflow and soil runoff increase nearly linearly with SnowF, mirroring the linear decline of direct snowmelt runoff

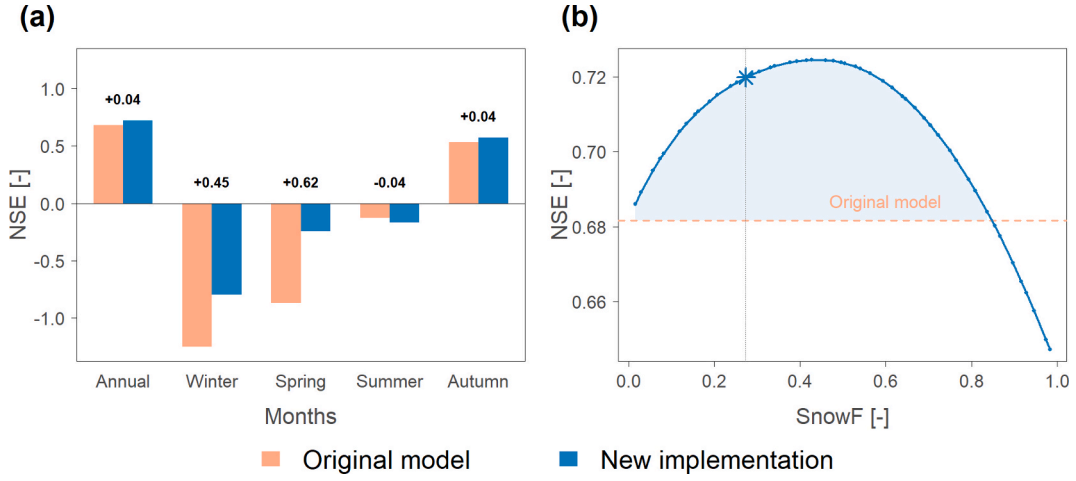


Fig. 6. Quantitative comparison of the original and improved SPHY model at Dupuli for daily discharge, 2005–2010. (a) Performance comparison for different temporal aggregation. (b) NSE of the improved structure across the full SnowF range from 50 Monte Carlo runs. The vertical line and star represent the SnowF calibrated value of 0.274.

(Fig. S10). The modified structure produced a higher NSE than the original one for all SnowF values below approximately 0.85, with a broad optimum between 0.25 and 0.65 that contains the calibrated value of 0.274. The improvement is therefore attributable to the added process representation rather than to the calibrated parameter value, and at Dupuli the modified structure outperforms the original model over almost the whole plausible range of SnowF.

4.3. Present-day hydrology and trends

At the outlet of the ZRB SPHY model domain, the mean annual water balance for 1991–2020 consists of 769 mm of precipitation, 137 mm (18%) of actual evapotranspiration and 664 mm of runoff (Fig. 7a). Rainfall accounts for 473 mm (61%) of the annual precipitation and snowfall for 296 mm (39%), although snowfall dominates the input from November to March. Runoff slightly exceeds the precipitation surplus over evapotranspiration, which is reflected in the small negative annual sum of the net flux (−32 mm yr^{-1}). About two thirds of this excess is glacier melt, which supplies water in addition to precipitation, and the remainder is a net depletion of basin storage. The monthly balance illustrates the storage and release regime of the basin. Between November and April the incoming fluxes exceed the outgoing fluxes, with a maximum net flux of + 61 mm $month^{-1}$ in March, as precipitation accumulates in the snowpack. Between May and October the release of this storage raises the outgoing fluxes above the concurrent input, with a minimum net flux of − 84 mm $month^{-1}$ in July, when runoff is about twice the monthly precipitation.

Snowmelt runoff is the dominant contributor (52.4%) to the total runoff, followed by baseflow (23.3%), rainfall-runoff (21.1%) and glacier melt (3.2%). The contribution of snowmelt runoff begins to rise in April and reaches its peak during June–July. Although the majority of precipitation falls as snow between October–April, melting peaks in June–July when temperatures are warmer. The snow contribution declines in winter, when temperatures are low and the solid fraction of precipitation is stored as snow at higher elevations in the ZRB. Baseflow is the second-largest contributor (23.3%) to the total runoff. The large baseflow contribution results from the considerable portion of snowmelt that infiltrates into the rootzone and subzone and eventually recharges to the groundwater layer in the model. Baseflow contributes to the river channel throughout the year, but its relative contribution increases in autumn and winter (September–February), when it sustains about half of the low winter flow. Rainfall-runoff contributes 21.1% of total runoff, peaking in July and declining rapidly thereafter. The glacier melt runoff contributes about 3.2% to the total runoff. Glacier ice melts when the surface temperature rises above zero, peaking in August once the seasonal snow cover on the glacier surface has depleted. Even though the annual contribution of glaciers is the smallest at the outlet, their monthly contribution reaches ~ 12% in September, when there is less water in the river system. The annual and seasonal runoff components show no significant trends (MK $p > 0.05$), whereas glacier melt runoff shows a significant declining trend at all time scales except the summer season (Fig. 7b). The strongest decline in glacier melt runoff trend occurs in autumn (−0.39 $m^3\ s^{-1}\ yr^{-1}$, MK $p < 0.05$). Seasonally the total runoff increases in spring and decreases in summer, winter and autumn, although none of these changes is significant at $p < 0.05$.

The spatial runoff patterns indicate that the snow and glacier melt runoff contribution dominates the upstream river reaches of the ZRB (Fig. 8). Glacier melt from the Zarafshon Glacier contributes ~ 70% of total runoff in the upper Matcha River, while snowmelt contributes ~ 90% for the upstream Fondarya River. Overall, the upstream ZRB catchment is mainly dominated by snowmelt runoff and glacier melt runoff. In the lower part of the basin, the flow is dominated by snowmelt runoff and baseflow.

4.4. Future changes

4.4.1. Changes in the cryosphere

All climate models project a decline in basin-aggregated snow persistence in the future relative to the reference period (Fig. 9). The difference from the reference snow persistence becomes larger for EoC compared with the MC time horizon. Furthermore, SSP585 projects a lower snow persistence compared with the reference and SSP126 and SSP370 (Fig. 9a-c). For example, the average snow persistence for the ZRB reduces from 0.59 to 0.46 (0.45) for MC and 0.45 (0.39) for the EoC

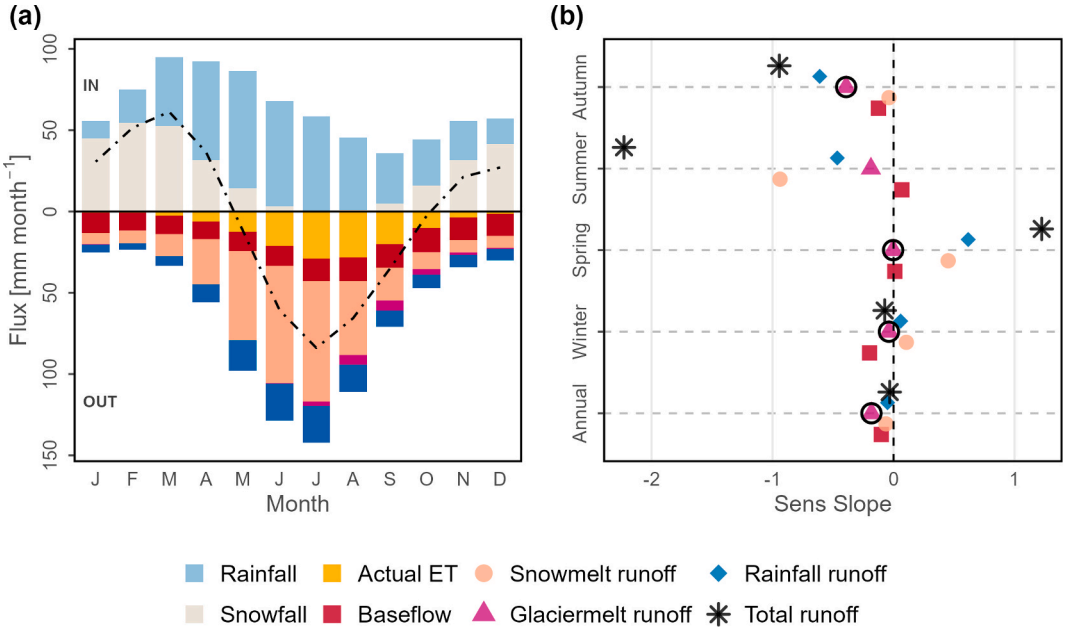


Fig. 7. (a) Monthly water balance of the Zarafshon River Basin at the outlet (just before the Zarafshon River enters Uzbekistan) for 1991–2020. Bars above the axis (IN) show the incoming fluxes; bars below the axis (OUT) show the outgoing fluxes, all expressed in mm $month^{-1}$ over the catchment area. The dot–dash line shows the monthly net flux (IN − OUT), representing the seasonal storage change of the snowpack, soil, and groundwater together with the excess glacier ice melt. (b) Linear trends of average seasonal (winter: DJF, spring:MAM, summer: JJA, autumn:SON) and annual runoff components (baseflow, snowmelt, glacier melt, and rainfall-runoff). Black circle represents trends that are significant (MK $p < 0.05$).

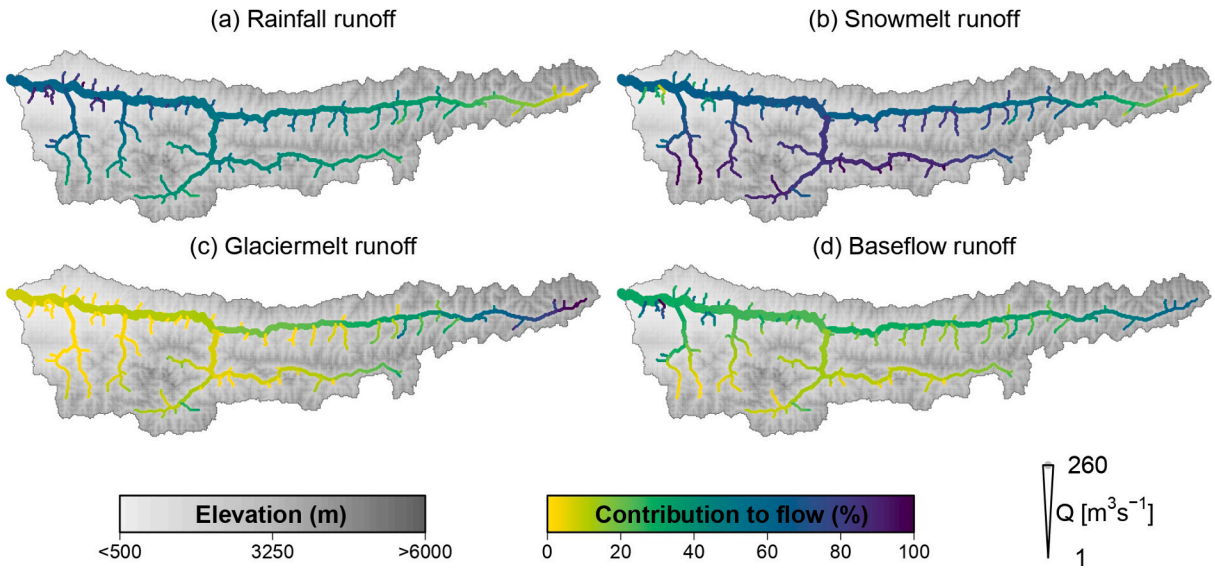


Fig. 8. Spatial contribution of flow components for the ZRB (just before the Zarafshon River enters Uzbekistan) for 1991–2020. (a) Rainfall-runoff (b) snowmelt runoff (c) glacier melt runoff and (d) baseflow. The background shows elevation; the color scale represents the contribution and the symbol size represents the discharge.

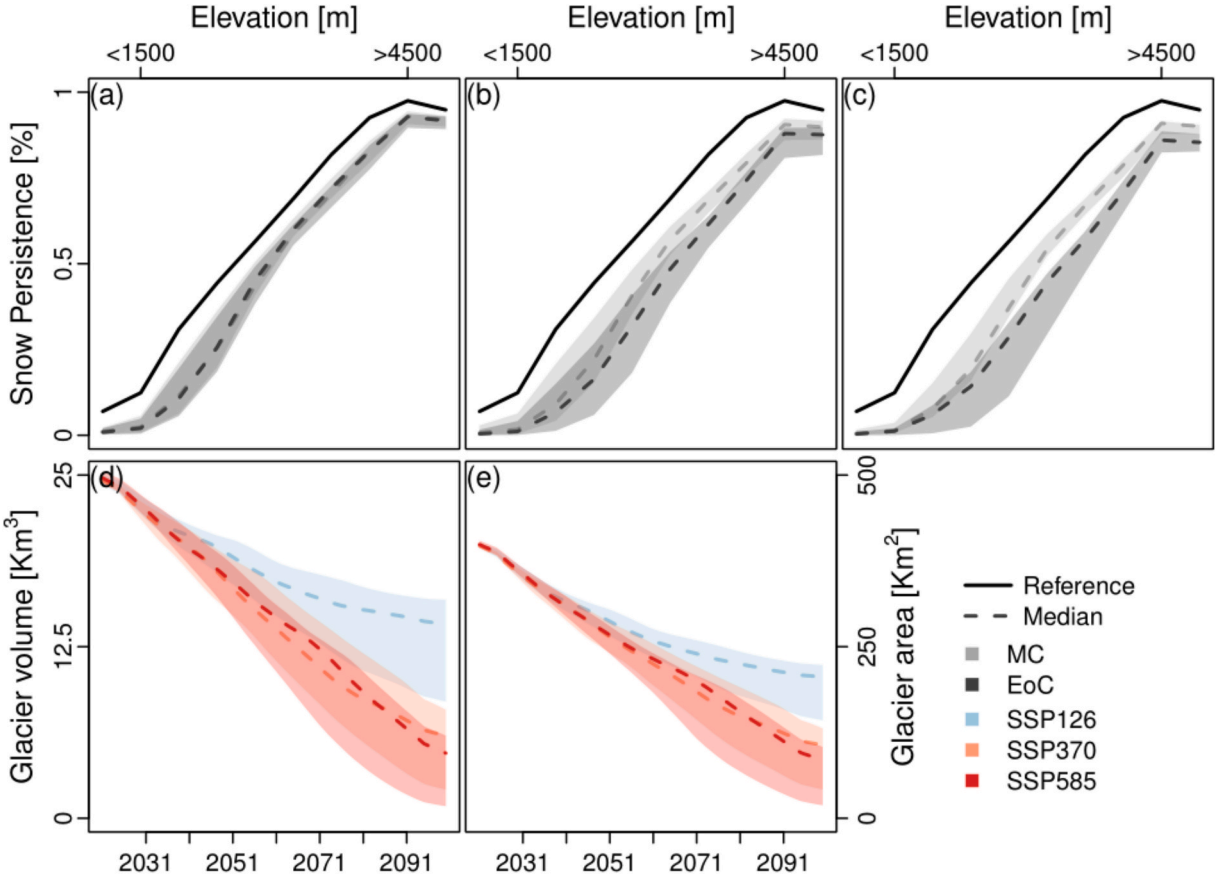


Fig. 9. Snow persistence per 500 m elevation band for the entire ZRB for reference, mid century (MC, 2036–2065) and end-of-century (EoC, 2071–2100) horizons for (a) SSP126 (b) SSP370 (c) SSP585 scenarios. Long-term changes in the (d) total volume and (e) area of all the glaciers in the ZRB (just before the Zarafshon River enters Uzbekistan) from 2021 to2100. The bandwidth represents the variability (minimum and maximum) of the five climate models within each SSP. The dashed line represents the median of the five climate models.

period for the SSP370 (SSP585) scenario, compared with the reference period. A reduction in solid precipitation, i.e. snowfall, due to enhanced warming is the main reason for declining snow persistence in the ZRB.

Glacier volume and area are projected to decline rapidly under all scenarios (Fig. 9d-e). Before 2040, the decline in area and volume in the SSP scenarios is rather similar. However, after 2040, the differences in

the different SSP scenarios become more prominent. The larger decrease in volume and glacier area in SSP585 compared with SSP126 is attributed to the warmer temperatures in SSP585. The magnitude of the decline of glacier volume and area is different for each scenario (Table S1). By 2070, ZRB glaciers are projected to lose roughly 50% of their 2020 vol under SSP370 and SSP585. By the EoC (2100), the SSP585 scenario results in a 79.6% volume loss, more than double the 38.6% loss projected under SSP126. A similar pattern is observed for the reduction in glacier area for the different SSP scenarios. For all SSP scenarios, the reduction in glacier area is larger compared with the reduction in volume of the glaciers (38.6% for glacier volume compared with 44.0% for glacier area under SSP126). This is because small glaciers, which hold little ice, disappear first.

4.4.2. Changes in water balance

The change in the phase of precipitation affects the entire water balance and not the melt components alone, under all three scenarios and in proportion to the warming (Table 5). By 2071–2100 the loss of snowfall increases from 25.5% under SSP126 to 38.2% under SSP370 and 46.9% under SSP585, and the rise in actual evapotranspiration from 19.0% to 41.2% and 51.7%. Total runoff is far less sensitive and declines by between 4.2% and 6.6% in all three, because the larger melt losses are offset by larger gains in rainfall-runoff and baseflow. Glacier melt runoff alone declines less under the warmer scenarios, by 42.9% under SSP585 compared with 74.5% under SSP126. Less ice remains under SSP585, yet it melts several times faster, because temperatures are higher and the reduced snowfall exposes bare ice earlier in the season.

Under SSP585, the warmest scenario, basin precipitation increases by 8% by 2071–2100 but its partitioning changes substantially (Fig. 10). Snowfall declines from 296 to 157 mm yr^{-1} and rainfall rises from 473 to 673 mm yr^{-1}, raising the rain share from 61% to 81%. Almost all of the additional rain falls between October and April, in the months that previously accumulated snow. Actual evapotranspiration increases from 137 to 208 mm yr^{-1} and baseflow from 155 to 212 mm yr^{-1}, because water that formerly accumulated in the snowpack and quickly drains off the catchment as melt runoff now infiltrates the root zone and drains to the channel through the groundwater compartment over a longer timescale. Snowmelt runoff falls by 48.2%, but the gains in rainfall-runoff (+55.5%) and baseflow largely offset this loss, so total runoff declines by only 6.3%. The annual total therefore changes little even though the flow paths that produce it change significantly.

4.4.3. Seasonal changes in hydrological regime

For MC and EoC, the ZRB is projected to experience substantial changes in its hydrological regime (both in magnitude and temporal shifts) across all SSPs, driven primarily by temperature-induced reductions in snowfall and runoff generation mechanisms (Fig. 11 and S11). Glacier melt runoff decreases in all SSP scenarios compared with the reference period for both horizons. Similarly, the snowmelt runoff declines across all SSP scenarios for both MC and EoC horizons, with greater changes in magnitude for EoC and a more pronounced decline under SSP585 compared with SSP126 and SSP370 (Table S2). The highest reduction in snowmelt runoff is observed in the autumn season followed by summer, winter and spring for EoC. By the EoC horizon, autumn snowmelt runoff is expected to decline by 32.9% (SSP126), 65.3% (SSP370), and 74.9% (SSP585) compared with the reference period. Whereas the total runoff in the future shows mixed seasonal patterns; as flows in winter and spring are consistently increasing and summer and autumn seasons are declining across all the scenarios. Winter total runoff shows the largest increase, projected at 16.5% (SSP126), 41.6% (SSP370), and 55.2% (SSP585). The increase in winter and spring runoff is primarily attributed to warming-induced higher proportions of liquid precipitation, generating rapid rainfall-runoff, and partly to earlier melting of seasonal snowpack.

Warming also affects the magnitude and timing of peak-runoff for total and component flows. Across both MC and EoC horizons and scenarios, peak-runoff for glacier melt, snowmelt, and total runoff decreases, while the rainfall-runoff peak increases (Table 6). During MC, glacier and snowmelt peak-runoff decline by 17.3–41.8% and 20.3–29.9%, respectively, whereas rainfall-runoff peak increases by 18.9–27.7%. By EoC, declines are larger: glacier and snowmelt peaks decrease by 34.3–65.4% and 25.6–47.3%, while rainfall-runoff peaks increase by 27.4–35.7%. Peak total runoff decreases by 22.6% under SSP585. Peak timing shifts earlier in all future horizons, by 22 ± 19 days (July to June) for SSP370 and 38 ± 17 days (July to May) for SSP585 at EoC.

4.4.4. Spatial changes in hydrological regime

Future climate induced warming has widespread and diverse impacts on the spatial patterns for the flow contributors (Fig. 12). The magnitude of the change is largest under SSP585 and the smallest under SSP126 (Fig. S12). Under SSP585 at the end-of-century the snowmelt contribution declines everywhere, but the decline grows steadily downstream. In the headwaters of the Matcha, downstream of the Zarafshon Glacier, it is about − 5 percentage points at Khudgif, reaching − 8 percentage points about halfway down the river. At Ayni, just before the Fondarya joins the Matcha, the changes are − 17.5 percentage points for snowmelt, −1.7 for glacier melt, +11.2 for rainfall-runoff and + 7.9 for baseflow. The same pattern occurs in the Fondarya just before the confluence but is larger, at − 19.5 for snowmelt, −2.4 for glacier melt, +12.6 for rainfall-runoff and + 9.4 for baseflow. The shift from snowmelt to rainfall-runoff is therefore stronger in the Fondarya than in the Matcha. Near Panjakent and at the outlet the changes are largest of all, −23.4 percentage points for snowmelt, +13.9 for rainfall-runoff, +10.8 for baseflow and − 1.2 for glacier melt.

4.4.5. Future changes in annual flows

The projected hydrological regime reveals divergent trends across SSP scenarios (Fig. 13). While historical trends are dominated by increasing rainfall-driven runoff, i.e. baseflow and rainfall-runoff, future projections diverge strongly with warming (Fig. 13a–c). For the SSP126 MC horizon all the runoff components, except glacier melt, show

Table 5
Annual water balance components of the Zarafshon River Basin at the basin outlet for the historical reference period 1991–2020 and for two 30-year future horizons, 2036–2065 and 2071–2100, under the SSP126, SSP370 and SSP585 scenarios. All fluxes are basin means in mm yr^{-1}, and the future values are multi-model means of the five CMIP6 GCMs. Values in parentheses give the relative change with respect to the reference period. Total runoff is the sum of the snowmelt, rainfall, glacier melt and baseflow contributions.

Period	Scenario	Snowfall	Rainfall	Actual ET	Snowmelt runoff	Rainfall-runoff	Glacier melt runoff	Baseflow	Total runoff
1991–2020	Reference	296	473	137	348	140	21	155	664
2036–2065	SSP126	235 (−20.7%)	601 (+27.0%)	159 (+16.4%)	276 (−20.8%)	188 (+34.3%)	10 (−54.7%)	195 (+25.9%)	668 (+0.7%)
2036–2065	SSP370	216 (−27.2%)	585 (+23.7%)	166 (+21.1%)	248 (−28.6%)	185 (+31.8%)	13 (−38.2%)	192 (+24.0%)	638 (−3.9%)
2036–2065	SSP585	208 (−29.7%)	612 (+29.3%)	172 (+25.3%)	244 (−30.0%)	195 (+39.3%)	14 (−33.0%)	198 (+27.9%)	651 (−2.0%)
2071–2100	SSP126	221 (−25.5%)	593 (+25.4%)	163 (+19.0%)	255 (−26.6%)	188 (+34.4%)	5(−74.5%)	187 (+20.9%)	636 (−4.2%)
2071–2100	SSP370	183 (−38.2%)	636 (+34.6%)	193 (+41.2%)	209 (−40.0%)	203 (+44.8%)	10 (−50.5%)	198 (+27.8%)	620 (−6.6%)
2071–2100	SSP585	157 (−46.9%)	673 (+42.3%)	208 (+51.7%)	180 (−48.2%)	218 (+55.5%)	12 (−42.9%)	212 (+37.0%)	622 (−6.3%)

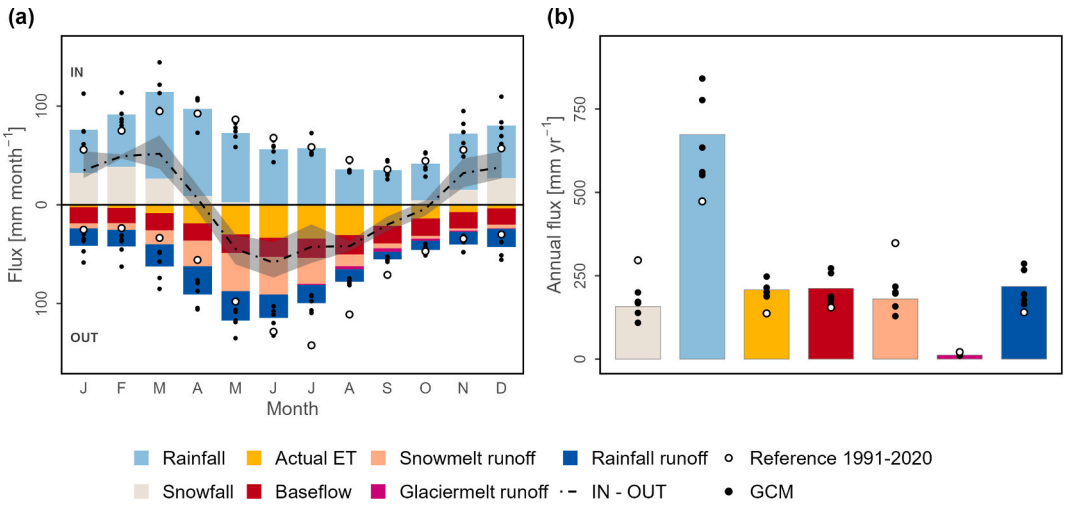


Fig. 10. Simulated water balance of the Zarafshon River Basin at the basin outlet under SSP585 for the end-of-century horizon (2071–2100). (a) Mean monthly water balance, with the incoming fluxes (IN) plotted above the zero line and the outgoing fluxes (OUT) below, expressed in mm month^{-1}. Stacked bars show the multi-model mean of the five GCMs and the black dots give the total IN and the total OUT of each GCM. The dot-dash line is the net flux (IN − OUT) and the grey band its range across the five models. (b) Annual totals of each flux, where the colored bars are the multi-model mean and the black dots the individual GCMs. Hollow circles in both panels mark the corresponding values for the historical reference period (1991–2020).

statistically significant decreasing trends (MK, $p < 0.05$) (Fig. 13d). The total annual runoff declines during the MC horizon (-1.55 m^3 s^{-1} yr^{-1}), driven primarily by reductions in snowmelt (-0.67 m^3 s^{-1} yr^{-1}). The flow contributors and total runoff increase over the EoC period (insignificant trend at $p < 0.05$ except for glacier melt). Under SSP370 for the MC horizon, the snowmelt runoff significantly decreases (-0.47 m^3 s^{-1} yr^{-1}) and consequently reduces the total runoff (Fig. 13e). The decreasing snowmelt runoff trend (-0.44 m^3 s^{-1} yr^{-1}) persists for the EoC horizon. The decreasing snowmelt trend is primarily due to the warming and decreasing snowfall.

In contrast, SSP585 produces a persistent and amplified decline in total runoff for EoC (-1.40 m^3 s^{-1} yr^{-1}) horizon, dominated by strong reductions in snowmelt runoff (MC:-0.61; EoC: -1.18 m^3 s^{-1} yr^{-1}) (Fig. 13f). Statistically significant trends (MK, $p < 0.05$) cluster for glacier melt and snowmelt runoff, highlighting cryospheric loss as the primary control on long-term total runoff decline. The results indicate a transition from snowmelt-driven to a rainfall-runoff dominated hydrological regime, with the strongest regime shift emerging under the SSP585 scenario.

5. Discussion

5.1. Flow contribution partitioning and comparison with other studies

There are no isotope or hydrochemistry-based hydrograph separation studies that have been published for the ZRB. The published ZRB-specific hydrological studies rely on discharge statistics rather than tracers (Groll et al., 2013; Olsson et al., 2010; Savoskul and Smakhtin, 2013). Our modeled partitioning of the runoff contributions is consistent with the statistical hydrograph separation studies, with the nearest tracer-based studies in the Tajik Pamirs and the Tien Shan, and with independent glacio-hydrological model studies of the Amu Darya and Syr Darya (Table S3). In all of the Central Asian studies compiled here, snowmelt is the dominant runoff source, and glacier melt is a minor annual contributor whose share scales with glacier cover. The flow contributions for the ZRB from this study (4.3% glacier cover resulting in 3.2% glacier melt, 52.4% snowmelt runoff and 21.1% rainfall-runoff) are of a similar order to those reported for the glacierized tributaries flowing into Lake Issyk-Kul (2–11% glacier cover resulting in 8–27% glacier melt, 50–64% snowmelt runoff and 7–23% rainfall-runoff) (Sadyrov et al., 2024), 6% glacier melt runoff and 47–52% snowmelt runoff in Gunt catchment with 7.5% glacier coverage (Huang et al., 2026), combined snow and ice melt runoff contribution of 27–46% in Gunt (Pohl et al., 2015), 10.3% glacier coverage in the Vakhsh resulting in 11.3% glacier melt runoff, 58.2% snowmelt runoff and 30.5% rainfall-runoff (Yan et al., 2026), the basin-wide estimates of Amu Darya (8% glacier melt runoff, 69% snowmelt runoff and 23% rainfall-runoff) and Syr Darya (2% glacier melt runoff, 74% snowmelt runoff and 23% rainfall-runoff) (Armstrong et al., 2019).

Isotope-based hydrograph separation across six Tian Shan catchments (930–22,925 km^2; glacier cover 0.3–17.4%) similarly indicated that snowmelt contributed 22–49% of total runoff during the typical snowmelt period and 12–59% during the typical glacier melt period (Chen et al., 2019). Based on these studies, we conclude that our results for runoff contributions are in the same ranges.

5.2. Shifting hydrological regimes

The reference period results for 1991–2020, show that the hydrological regime is governed by snowmelt, in which snow and glacier melt dominate the upstream areas and rainfall-runoff and baseflow sustain the flow in the lower reaches. The hydrological regime shows considerable annual variability due to changes in precipitation, temperature, and snow and glacier reserves. Over the past three decades, glacier melt has demonstrated a statistically significant declining trend, driven predominantly by rising temperatures. The results align with the negative mass balance of -0.32 ± 0.37 m w.e. yr^{-1} reported for the Pamir-Alay by Barandun & Pohl (2023) and with the area loss observed in the upper Zarafshon basin by Halimov et al. (2026).

The glacier loss projections from this study, 79.6% under SSP585 compared with 38.6% under SSP126 by 2100, are consistent with regional projections, although they lie at the upper end of the published range. Rounce et al. (2020) project losses of 29 ± 12% under RCP2.6 and 67 ± 10% under RCP8.5 for High Mountain Asia, and state that the Pamir-Alay is expected to lose more mass than other regions because it becomes warmer without becoming wetter. Kraaijenbrink et al. (2017) project a loss of approximately 36% of the present-day ice mass under a global warming of 1.5 °C, which is close to the loss simulated here for SSP126. Lyu et al. (2026) find peak water for the Pamir and Hissar-Alay after the 2050 s under SSP585, which is consistent with the mid-century maximum of glacier melt simulated in this study.

These changes will substantially alter the hydrological regime, with

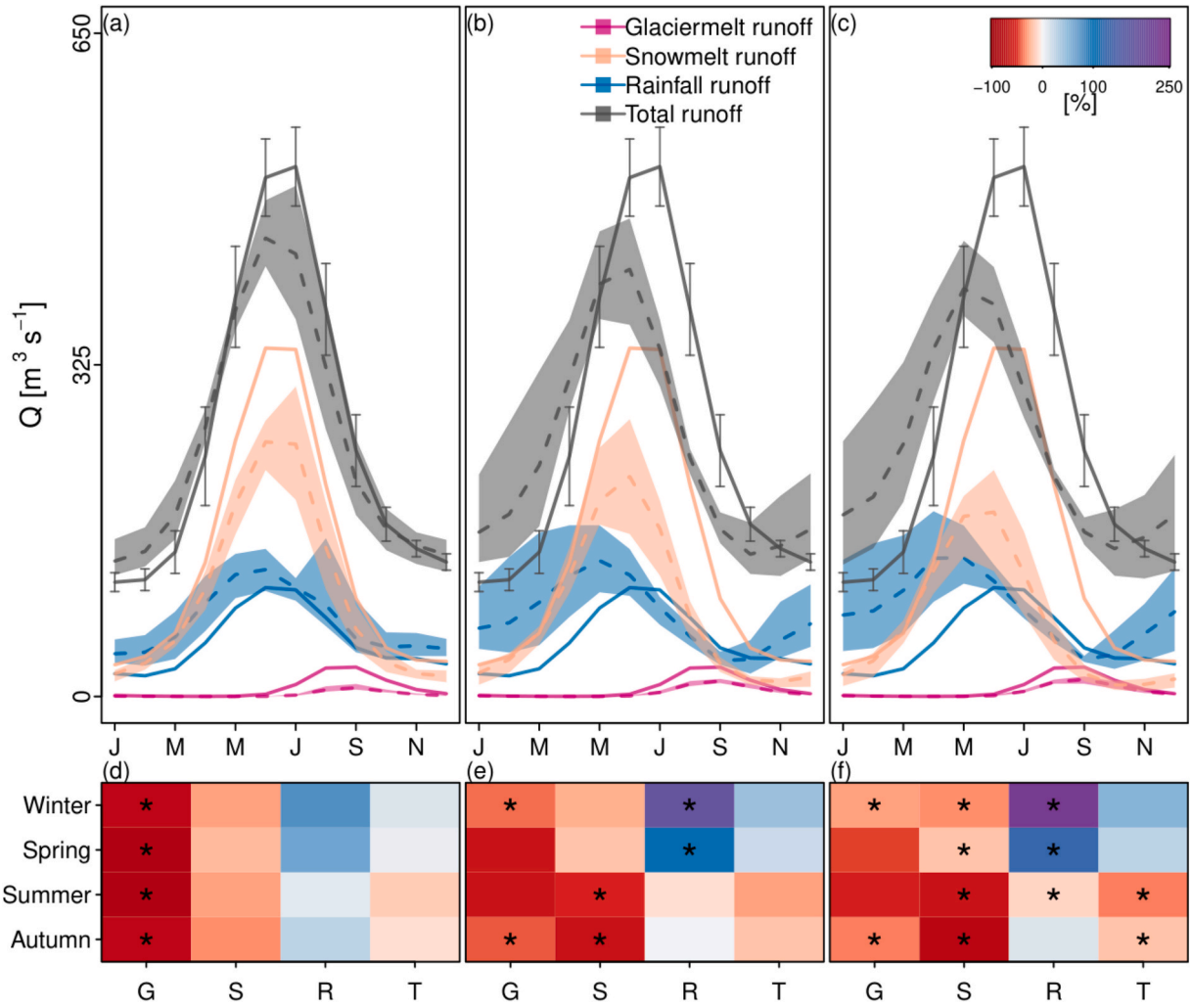


Fig. 11. Climatological changes in the hydrological regime for the end-of-century (EoC, 2071–2100) at the outlet of the ZRB (just before the Zarafshon River enters Uzbekistan). The top and bottom panels represent three Shared Socioeconomic Pathways, i.e. (a,d) SSP126, (b,e) SSP370 and (c,f) SSP585. The shaded color represents the variability (minimum and maximum) of the flow contributors. The dashed and solid colored lines represent the mean of the five climate models and the reference period (1991–2020), respectively. Error bars on the reference total runoff show ± 1 standard deviation across the ten best-performing Monte Carlo calibration parameter sets (1991–2020), plotted about the reference simulation. The bottom three heat map panels represent the percent change in the mean seasonal simulated runoff (Winter-DJF, Spring-MAM, Summer-JJA, Autumn-SON) of the five climate models compared with the reference period (1991–2020) for the different runoff variables (G for glacier melt runoff, S for Snowmelt runoff, R for rainfall-runoff and T for total runoff). Black asterisks represent changes that are significant (MK $p < 0.05$).

glacier melt and snowmelt contributing less, while rainfall-runoff will contribute more to the discharge. A transition from glacial-nival (melt-dominant) to a nival-pluvial dominant regime has been reported by several other regional studies. Murodov et al. (2025) for the Vanj River basin and Hou et al. (2025) for the Amu Darya River basin project a declining meltwater share and a growing rainfall-runoff contribution. Li et al. (2020) show that the snowfall fraction in the alpine regions of Central Asia has declined since 1998, most strongly between 1,500 and 3,500 m, the elevation band that contributes to most of the snowmelt in the ZRB. Hou et al. (2025) project a sharp decline of snowmelt in the Amu Darya basin together with a growing rainfall contribution and a loss of the glacial buffering effect. Zhang et al. (2026) project that the glacier contribution to runoff becomes negligible by EoC in basins with low to moderate glacier cover.

Results project a shift in the annual peak discharge, 22 ± 19 days (from July to June) and 38 ± 17 days (July to May) for the SSP370 and SSP585 for EoC horizon. Comparable shifts of the summer maximum runoff toward spring have been projected for the Tien Shan (Sorg et al., 2014, 2012) and for the neighboring Gunt catchment in the Pamir (Pohl et al., 2017). Gulakhmadov et al. (2020) project a shift of the peak flow month from July to June in the Vakhsh basin under both RCP4.5 and RCP8.5. Didovets et al. (2021) report a shift of the peak of river discharge of up to one month for eight CA catchments, together with a shortening of the snow accumulation period. Kalashnikova et al. (2023) project shifts from July to June in glacier-snow-fed rivers and from June to May in snow-glacier-fed rivers, and cite a range of 15 to 50 days for Kyrgyz basins. For the Amu Darya, Khanal et al. (2021) project a shift of the peak of total runoff from June to April or May. The magnitude of the shift simulated here for the ZRB falls within this range. The direction is also consistent with the observations of Olsson et al. (2010), who reported a reduced summer flood and increased spring flows in the Zarafshon.

The changes are not uniform over the ZRB. For the Fondarya, the shift in the hydrological regime away from snowmelt dominance is larger than for the Matcha River system. Under reference conditions, snowmelt contributes 63.5% of runoff in the Fondarya compared with 52.8% in the Matcha. Both receive roughly 7% more precipitation by the EoC and show an 80% increase in actual evapotranspiration relative to the reference period, yet annual runoff declines three times more strongly in the Fondarya (13.2%) than in the Matcha (4.2%). This is

Table 6
Changes in the peak-runoff, expressed as the percentage change relative to the reference period, of the contributors (G for glacier melt runoff, S for Snowmelt runoff and R for rainfall-runoff) and total runoff (T) for mid-century (MC, 2036–2065) and end-of-century (EoC, 2071–2100) horizons at the outlet of the ZRB (just before the Zarafshon River enters Uzbekistan). The '-' value indicates a decrease (or earlier compared with the reference time) and '+' indicates an increase (or later compared with reference time) in peak-runoff. The last column represents the shift in peak total runoff in days. All the values are computed using the daily climatologies. The values in parentheses represent the ± 1 standard deviation.

		G	R	S	T	Shift in peak total runoff (days)
MC	SSP126	−41.8 (11.2)	+18.9 (5.9)	−20.3 (9.6)	−8.2 (8.0)	−3 (8)
	SSP370	−22.9 (10.5)	+20.8 (17.1)	−28.5 (8.0)	−14.3 (5.5)	−3 (6)
	SSP585	−17.3 (13.3)	+27.7 (10.5)	−29.9 (6.5)	−13.6 (6.5)	−6 (2)
EoC	SSP126	−65.4 (9.1)	+30.0 (16.7)	−25.6 (9.7)	−12.9 (7.2)	−3 (8)
	SSP370	−40.4 (7.1)	+27.4 (26.8)	−38.7 (11.0)	−19.5 (6.5)	−22 (19)
	SSP585	−34.3 (10.1)	+35.7 (28.5)	−47.3 (9.3)	−22.6 (4.8)	−38 (17)

primarily due to a combination of differences in hypsometry, rain–snow partitioning and glacier cover.

Reference snowfall fractions in the Fondarya exceed those in the Matcha at every elevation (45.4% against 38.6% at 2,500–3,000 m, and 59.0% against 51.3% at 3,000–3,500 m). By EoC under SSP585, the basin-wide snowfall fraction declines by 24.1 percentage points in the Fondarya and by 19.3 in the Matcha, although snowmelt remains the largest runoff source in both sub-basins (44.0% and 35.3%, respectively). Only 10.1% of the Fondarya lies above 4000 m, compared with 19.0% of the Matcha, and glaciers cover 2.82% and 9.12% of the two sub-basins, respectively. The Fondarya contains no glacier larger than 3.5 km^2, and 94% of its 287 glaciers are smaller than 1 km^2 (RGI Consortium, 2017). The Matcha contains six glaciers larger than 10 km^2, including the Zarafshon Glacier (87.2 km^2), which account for 40% of its glacierised area and an estimated 70% of its ice volume.

Glacier melt runoff declines by 97.1% in the Fondarya (from 15.62 to 0.46 mm yr^{-1}) and 26.9% in the Matcha (43.09 to 31.48 mm yr^{-1}) by EoC under SSP585, reducing the glacier contribution to annual runoff from 2.5% to 0.1% and from 7.1% to 5.4%, respectively. Projected increases in rainfall-runoff and baseflow offset 80% of the combined snowmelt and glacier melt loss in the Matcha but only 52% in the Fondarya. Therefore, annual total runoff declines by 4.2% in the Matcha and 13.2% in the Fondarya. These results show that the shift toward a more rainfall-dominated regime is uneven across the ZRB, so that a basin-wide average simplifies the order in which individual tributaries change. For water management the earlier and lower peak is more consequential than the change in annual volume, because irrigation demand in the lower basin coincides with the late-summer flows that decline first.

5.3. *Downstream impacts and adaptation*

Snowmelt and glacier melt deliver a steady water supply during spring and early summer, as well as during dry periods, which ensures a reliable water supply for crop irrigation (Biemans et al., 2019). The hydrological changes — the reduction in magnitude of total flow and shift in the peak total flow — will affect the downstream water users (Immerzeel et al., 2020; Viviroli et al., 2026). CA has been identified as one of the global hotspots where irrigated agriculture depends most strongly on snowmelt, and where up to 40% of irrigation demand may have to be met from alternative sources (Qin et al., 2020). Water scarcity in the Amu Darya basin is projected to increase further under continued warming (Yao et al., 2022), while crop water consumption in the basin has already risen by about 10% since the late 1980 s, and shifts towards less water-intensive crops have offset only a small fraction of this increase (Pena-Guerrero et al., 2026).

For the agriculture sector, a shift from a snowmelt-dominated to a rainfall-runoff dominated hydrological regime means that the timing and availability of water for crops will change (Siegfried et al., 2012). In particular the small and medium-hold farmers in the mountains with significant dependence on snowmelt (e.g. along the Matcha and in the Fondarya sub-basin) and high exposure with limited adaptive capacity will be vulnerable to these seasonal changes (Xenarios et al., 2019). This shift may require farmers to invest in additional water storage, improve irrigation efficiency, adjust planting schedules, and adopt drought-

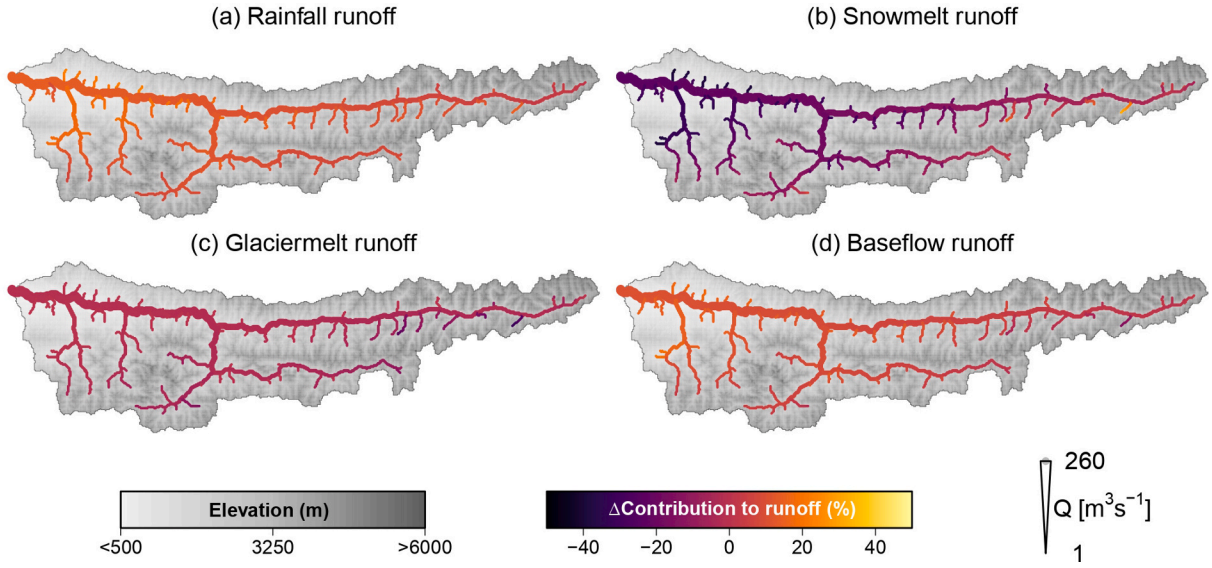


Fig. 12. Difference in contribution to total runoff [%], compared with the reference period (1991–2020), for the SSP585 scenario and EoC (2071–2100) horizon for (a) Rainfall-runoff (b) snowmelt runoff (c) glacier melt runoff and (d) baseflow runoff. The background shows elevation; the color scale represents the difference in contribution and the symbol size represents the discharge. Negative (positive) values indicate a decrease (increase) in the future contribution relative to the reference period.

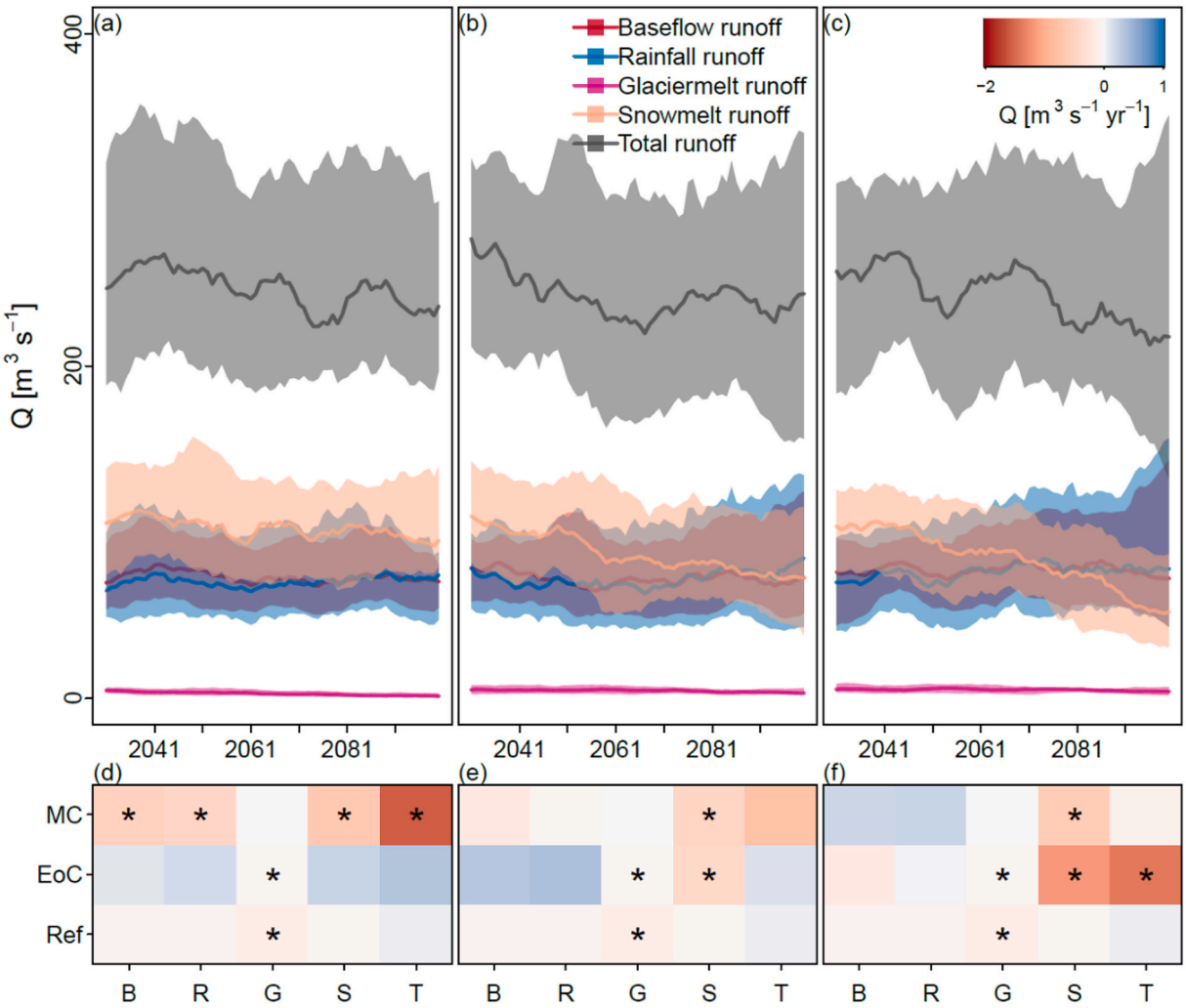


Fig. 13. Annual hydrological regime at the outlet of the ZRB (just before the Zarafshon River enters Uzbekistan). The top and bottom panels represent three Shared Socioeconomic Pathways, i.e. (a,d) SSP126, (b,e) SSP370 and (c,f) SSP585. In the top row, the solid colored line represents the median of the five climate models and the shading represents the variability of the flow components (baseflow, rainfall-runoff, glacier melt, snowmelt and total runoff) across the five models, shown as a 10-year running mean for 2031–2100. The bottom three heat map panels represent the trend (Sen's slope) of annual simulated runoff for different runoff variables (B for baseflow runoff, G for glacier melt runoff, S for Snowmelt runoff, R for rainfall-runoff and T for total runoff). Black asterisks mark trends that are significant (Mann-Kendall $p < 0.05$).

tolerant crops (Abdullaev and Rakhmatullaev, 2016; Mukhamedjanov et al., 2021). Adaptive management is therefore essential to maintain agricultural productivity under a changing regime (Pahl-Wostl, 2007). Initiatives such as the International Year of Glaciers' Preservation 2025 and the Decade of Action for Cryospheric Sciences (2025–2034), led by the United Nations, can serve as catalysts to support science, practice, and policy development aimed at building resilience to climate change in Central Asian river basins.

5.4. Limitations and recommendations

The results in this study are based on ERA5 reanalysis data downscaled using the TopoSCALE approach, which, despite bias corrections applied for temperature and precipitation, exhibits large uncertainties in mountainous basins such as the Zarafshon basin. The ability to use station observations to correct gridded meteorological data remains limited by the sparse observational network in Central Asia, particularly in the mountainous regions of Tajikistan. In particular, the number of precipitation gauges located at high altitude, where most precipitation occurs, is limited. The scarcity of meteorological, cryospheric and hydrological observations hampers more robust calibration and validation of glacio-hydrological models. Future research should prioritize the development of a homogenised and representative reference climate data archive for Zarafshon and Central Asia.

In addition, the uncertainty in the future climate remains large, as demonstrated by the large range in climate projections. The applicability of climate projections generated by large scale General Circulation Models for climate change impacts in mountainous terrain remains challenging, despite downscaling efforts. Improved representations of mountainous climate in general circulation models and regional climate models may provide higher certainty in climate projections for mountainous river basins such as the ZRB.

Sublimation from the seasonal snowpack is not represented in the model. Studies in the Himalaya report sublimation losses in the order of 10–20% of annual snowfall (Mandal et al., 2022; Stigter et al., 2018). Similar losses are plausible above 4,000 m in ZRB and Central Asia (Jianqiao et al., 2025; Zhu et al., 2020). The corrected precipitation approach used in this study, constrained by the observed discharge, represents the net water input that is available for runoff rather than the true gross precipitation. Therefore, the actual snowfall at high elevations is likely somewhat larger than the amount reported in this study. Permafrost is expected to occur above approximately 3,500 m in ZRB

(Barandun et al., 2020; Mathys et al., 2025). Permafrost dynamics, including ground ice, frozen-ground effects on infiltration, and thaw-related changes in storage, are likewise not resolved currently by SPHY. Their exclusion may affect the simulated baseflow seasonality, although part of this effect is included in the calibration of the groundwater parameters. Permafrost degradation under warming increases subsurface storage and hydraulic connectivity, which would partly offset the projected decline in summer baseflow and delay the recession; the projections of late-summer low flow presented here are therefore likely to be conservative. Neither process changes the sign of the projected regime shift, because both act on the timing and storage of meltwater rather than on the rain-snow partitioning that drives the shift, but they widen the uncertainty of the summer and autumn projections provided in this study. Future research should also focus on improving the simulation of other key physical processes that the model does not resolve, including snow avalanching, sublimation, permafrost, glacier dynamics (e.g., debris cover, ponds, cliffs), groundwater processes, and flow routing.

The simulated glacier evolution carries forward the uncertainty of its input data and of the redistribution scheme. Initial ice thickness is taken from the consensus estimate of Farinotti et al. (2019), whose per-glacier uncertainty propagates directly into the projected volume loss and into the timing at which individual glaciers disappear. Glacier outlines are a single Randolph Glacier Inventory snapshot (RGI Consortium, 2017), so the initial glacierised area is fixed at the inventory date. Debris cover is a binary classification derived following Kraaijenbrink et al. (2017) and carries no debris thickness, so its insulating effect can only be represented in an aggregated way. The accumulation side of the mass balance is not constrained by observations. No snow water equivalent measurements exist for the ZRB, and the MODIS snow cover used in the calibration is a binary extent that becomes insensitive to snowpack depth once the ground is fully covered. The annual redistribution moves the surplus from the accumulation zone to the ablation zone in a single step, in proportion to the ice volume already present, and contains no ice flow. The dynamic response time of each glacier is therefore not resolved, and the derived surface mass balance additionally assumes constant firn densification. Propagating these uncertainties was beyond the scope of this study, and the projected glacier decline should be read as a single realisation rather than a bounded range. Future work should propagate an ensemble of ice thickness estimates, use debris thickness observations, obtain direct snow water equivalent measurements at high elevation, and couple the model to a dynamic ice-flow scheme.

This study uses a simplified spatially uniform implementation of SnowF. Infiltration of snowmelt depends on soil texture and depth, slope, vegetation and the frozen state of the ground, and would be expected to be higher on the deep alluvial and talus deposits of the valley floors than on the thin soils and bedrock of the high ridges. Distributing SnowF according to the HiHydroSoil hydraulic properties or constraining it with isotope data should be prioritised in the future work.

The sensitivity analysis also shows the limits of the calibration itself. Only three parameters are clearly constrained by the available observations, and the remaining six can take almost any value within their sampled ranges without degrading performance. The selected run is therefore one member of a larger set of equally acceptable parameter sets. Future work could focus on propagating the full set of best-performing runs through the climate projections to quantify this parameter uncertainty. Additional observations, such as remotely sensed evapotranspiration or a dedicated isotope sampling campaign, would help to constrain the parameters that discharge, snow cover and glacier mass balance currently leave undetermined.

6. Conclusions

We quantified present-day and future hydrological regime change in the Zarafshon River Basin using the SPHY glacio-hydrological model. Our main findings are:

- Our model improvements redistribute water from direct snowmelt runoff to delayed baseflow and improve model performance in winter and spring relative to the original SPHY formulation. We calibrated the improved model simultaneously against discharge, MODIS snow cover and altitudinal glacier mass balance, using a Monte Carlo procedure with a multi-objective function. The selected parameter set is one member of a larger set of equally acceptable solutions.
- The historical analysis (1991–2020) shows that precipitation accumulates as snow between November and April and is released between May and October, when runoff exceeds the precipitation. Snowmelt is the dominant runoff source contributing about half of total discharge, followed by baseflow and rainfall-runoff. Glacier melt contributes a relatively small share annually, but plays an important buffering role during late summer low-flow periods. Snow and glacier melt dominate the upstream headwaters, while baseflow and rainfall-runoff become increasingly important downstream.
- Snow persistence and glacier volume are projected to decrease under all SSP scenarios, with glacier volume losses reaching ~ 80% by the end-of-century under SSP585. As a result, snowmelt and glacier melt runoff decline strongly, particularly in summer and autumn. Future projections indicate a substantial shift from a melt-dominated to a rainfall-runoff-dominated regime, driven by warming-induced cryospheric decline. Warming shifts precipitation from snow to rain, so snowmelt runoff declines sharply while rainfall-runoff and baseflow increase. These gains almost compensate for the melt losses, and total annual runoff declines by less than 7% under all scenarios. The cryospheric components show significant trends ($p < 0.05$), which identify cryospheric loss as the dominant control on the long-term decline in runoff.
- Across horizons and scenarios, peak-runoff from glacier melt and snowmelt decreases, whereas peak rainfall-runoff increases. Under SSP585, peak total runoff declines by 22.6% by the end-of-century and the annual discharge maximum shifts from July toward June and May. The hydrological regime shift is uneven within the basin. Annual runoff declines three times more strongly in the Fondarya than in the Matcha, as Fondarya has a smaller share of its area at high elevation, a larger snowfall fraction to lose at every elevation, and too little ice to buffer that loss. The Matcha retains substantial glacier storage, including the Zarafshon Glacier, which compensates part of its snowmelt decline.
- These changes will have important consequences for downstream water availability and irrigation-dependent agriculture in Tajikistan and Uzbekistan. Reduced summer flows and an earlier peak coincide with the critical crop growing period, so changes in both timing and volume matters for water management. Despite the uncertainties from climate projections and data scarcity, this study shows the value of explicitly resolving cryospheric flow components to inform climate adaptation and long-term water security planning in Central Asian mountainous river basins.

CRediT authorship contribution statement

Sonu Khanal: Writing – original draft, Investigation, Funding acquisition, Formal analysis, Data curation, Conceptualization, Methodology, Project administration, Software, Validation, Visualization, Writing – review & editing. **Philip Kraaijenbrink:** Writing – review & editing, Methodology, Formal analysis, Data curation. **Faezeh Nick:** Writing – review & editing, Investigation, Data curation. **Joel Fiddes:** Writing – review & editing, Data curation. **Arthur Lutz:** Writing – review & editing. **Evan Miles:** Data curation. **Esteban Garcia:** Writing – review & editing. **Brecht Haeyer:** Writing – review & editing. **Johannes Hunink:** Writing – review & editing. **Walter Immerzeel:** Writing – review & editing, Supervision, Methodology.

Declaration of competing interest

The authors declare that they have no known competing financial interests or personal relationships that could have appeared to influence the work reported in this paper.

Acknowledgements

This research was financially supported by the Integrated Rural Development Project / TRIGGER which is co-funded by the European Union and the German Federal Ministry for Economic Cooperation and Development (BMZ), and implemented by the Deutsche Gesellschaft für Internationale Zusammenarbeit (GIZ) GmbH under grant ID 81293815a. The authors would like to thank the National Water and Information System under the Ministry of Energy and Water Resources of Tajikistan and Zarafshon River Basin Organization for providing the meteorological and hydrological information to calibrate and validate the hydrological model.

Appendix A. Supplementary data

Supplementary data to this article can be found online at https://doi.org/10.1016/j.jhydrol.2026.136676.

Data availability

Data will be made available on request.

References

Aalstad, K., Westermann, S., Schuler, T.V., Boike, J., Bertino, L., 2018. Ensemble-based assimilation of fractional snow-covered area satellite retrievals to estimate the snow distribution at Arctic sites. Cryosphere 12, 247–270. https://doi.org/10.5194/TC-12-247-2018.

Aalto, J., Kämäräinen, M., Shodmonov, M., Rajabov, N., Venäläinen, A., 2017. Features of Tajikistan's past and future climate. Int. J. Climatol. 37, 4949–4961. https://doi.org/10.1002/joc.5135.

Abdullaev, I., Rakhmatullaev, S., 2016. Setting up the agenda for water reforms in Central Asia: does the nexus approach help? Environ. Earth Sci. 75, 870. https://doi.org/10.1007/s12665-016-5409-8.

Abdushukurov, D.A., Abdusamadzoda, D., Duliu, O.G., Zinicovscaia, I., Nekhoroshkov, P. S., 2022. On the geochemistry of major and trace elements distribution in sediments and soils of Zarafshon River Valley, Western Tajikistan. Appl. Sci. Switz. 12. https://doi.org/10.3390/app12062763.

Armstrong, R.L., Rittger, K., Brodzik, M.J., Racoviteanu, A., Barrett, A.P., Khalsa, S.-J.-S., Raup, B., Hill, A.F., Khan, A.L., Wilson, A.M., Kayastha, R.B., Fetterer, F., Armstrong, B., 2019. Runoff from glacier ice and seasonal snow in High Asia: separating melt water sources in river flow. Reg. Environ. Chang. 19, 1249–1261. https://doi.org/10.1007/s10113-018-1429-0.

Barandun, M., Fiddes, J., Scherler, M., Mathys, T., Saks, T., Petrakov, D., Hoelzle, M., 2020. The state and future of the cryosphere in Central Asia. Water Secur. 11, 100072. https://doi.org/10.1016/j.wasec.2020.100072.

Barandun, M., Pohl, E., 2023. Central Asia's spatiotemporal glacier response ambiguity due to data inconsistencies and regional simplifications. Cryosphere 17, 1343–1371. https://doi.org/10.5194/tc-17-1343-2023.

Barandun, M., Pohl, E., Naegeli, K., McNabb, R., Huss, M., Berthier, E., Saks, T., Hoelzle, M., 2021. Hot spots of glacier mass balance variability in Central Asia. Geophys. Res. Lett. 48, e2020GL092084. https://doi.org/10.1029/2020GL092084.

Beven, K., 2001. How far can we go in distributed hydrological modelling? Hydrol. Earth Syst. Sci. 5, 1–12. https://doi.org/10.5194/hess-5-1-2001.

Biemans, H., Siderius, C., Lutz, A.F., Ahmad, B., Hassan, T., Bloh, W.V., Wijngaard, R.R., Wester, P., Shrestha, A.B., Immerzeel, W.W., 2019. Importance of snow and glacier meltwater for agriculture on the Indo-Gangetic Plain. Nat. Sustain. 2. https://doi.org/10.1038/s41893-019-0305-3.

Bisset, R.R., Dehecq, A., Goldberg, D.N., Huss, M., Bingham, R.G., Gourmelen, N., 2020. Reversed Surface-Mass-Balance Gradients on Himalayan Debris-Covered Glaciers Inferred from Remote Sensing. Remote Sens. 2020 Vol 12 Page 1563 12, 1563. https://doi.org/10.3390/RS12101563.

Chen, C., Zhang, X., Lu, H., Jin, L., Du, Y., Chen, F., 2021. Increasing summer precipitation in arid Central Asia linked to the weakening of the East Asian summer monsoon in the recent decades. Int. J. Climatol. 41, 1024–1038. https://doi.org/10.1002/joc.6727.

Chen, H., Chen, Y., Li, W., Li, Z., 2019. Quantifying the contributions of snow/glacier meltwater to river runoff in the Tianshan Mountains. Central Asia. Glob. Planet. Change 174, 47–57. https://doi.org/10.1016/j.gloplacha.2019.01.002.

Chen, Y., Li, W., Deng, H., Fang, G., Li, Z., 2016. Changes in Central Asia's water tower: past, present and future. Sci. Rep. 6, 1–12. https://doi.org/10.1038/srep35458.

Dahri, Z.H., Ludwig, F., Moors, E., Ahmad, S., Ahmad, B., Ahmad, S., Riaz, M., Kabat, P., 2021. Climate change and hydrological regime of the high-altitude Indus basin under extreme climate scenarios. Sci. Total Environ. 768, 144467. https://doi.org/10.1016/J.SCITOTENV.2020.144467.

Didovets, I., Lobanova, A., Krysanova, V., Menz, C., Babagalieva, Z., Nurbatsina, A., Gavrilenko, N., Khamidov, V., Umirbekov, A., Qodirov, S., Muhyyew, D., Hattermann, F.F., 2021. Central Asian rivers under climate change: impacts assessment in eight representative catchments. J. Hydrol.: Reg. Stud. 34, 100779. https://doi.org/10.1016/j.ejrh.2021.100779.

Ding, Y., Zhang, S., Chen, R., Han, T., Han, H., Wu, J., Li, X., Zhao, Q., Shangguan, D., Yang, Y., Liu, J., Wang, S., Qin, J., Chang, Y., 2020. Hydrological basis and discipline system of cryohydrology: from a perspective of cryospheric science. Front. Earth Sci. 8, 566. https://doi.org/10.3389/FEART.2020.574707/BIBTEX.

Farinotti, D., Huss, M., Fürst, J.J., Landmann, J., Machguth, H., Maussion, F., Pandit, A., 2019. A consensus estimate for the ice thickness distribution of all glaciers on Earth. Nat. Geosci. 12, 168–173. https://doi.org/10.1038/s41561-019-0300-3.

Farinotti, D., Longuevergne, L., Moholdt, G., Duethmann, D., Mölg, T., Bolch, T., Vorogushyn, S., Güntner, A., 2015. Substantial glacier mass loss in the Tien Shan over the past 50 years. Nat. Geosci. 8, 716–722. https://doi.org/10.1038/ngeo2513.

Farr, T.G., Rosen, P.A., Caro, E., Crippen, R., Duren, R., Hensley, S., Kobrick, M., Paller, M., Rodriguez, E., Roth, L., Seal, D., Shaffer, S., Shimada, J., Umland, J., Werner, M., Oskin, M., Burbank, D., Alsdorf, D., 2007. The shuttle radar topography mission. Rev. Geophys. 45. https://doi.org/10.1029/2005RG000183.

Fiddes, J., Aalstad, K., Westermann, S., 2019. Hyper-resolution ensemble-based snow reanalysis in mountain regions using clustering. Hydrol. Earth Syst. Sci. 23, 4717–4736. https://doi.org/10.5194/HESS-23-4717-2019.

Fiddes, J., Endrizzi, S., Gruber, S., 2015. Large-area land surface simulations in heterogeneous terrain driven by global data sets: application to mountain permafrost. Cryosphere 9, 411–426. https://doi.org/10.5194/TC-9-411-2015.

Fiddes, J., Gruber, S., 2014. TopoSCALE vol 1.0: downscaling gridded climate data in complex terrain. Geosci. Model Dev. 7, 387–405. https://doi.org/10.5194/gmd-7-387-2014.

Gafforzoda, I.G., Arabov, F.P., Sodikov, A.K., 2023. Sustainable development of water resources of Tajikistan. IOP Conf. Ser.: Earth Environ. Sci 1229, 012024. https://doi.org/10.1088/1755-1315/1229/1/012024.

Geweke, J., 1998. Efficient simulation from the multivariate normal and student-t distributions subject to linear constraints and the evaluation of constraint probabilities. Comput. Sci. Stat 23.

Groll, M., Opp, C., Kulmatov, R., Ikramova, M., Normatov, I., 2013. Water quality, potential conflicts and solutions—an upstream–downstream analysis of the transnational Zarafshan River (Tajikistan, Uzbekistan). Environ. Earth Sci. 73, 743–763. https://doi.org/10.1007/s12665-013-2988-5.

Gulakhmadov, A., Chen, X., Gulahmadov, N., Liu, T., Anjum, M.N., Rizwan, M., 2020. Simulation of the potential impacts of projected climate change on streamflow in the Vakhsh River Basin in Central Asia under CMIP5 RCP scenarios. Water 12, 1426. https://doi.org/10.3390/w12051426.

Halimov, A., Li, J., Safarov, M., Sheralizoda, N., Li, R., Nasrulloev, F., Shoergashova, S., Murodkhudzha, M., 2026. Detecting glacier dynamics during 2016–2024 using planet imagery in the upper Zarafshon River Basin, Tajikistan. Remote Sens. 18, 1293. https://doi.org/10.3390/rs18091293.

Hall, D.K., Riggs, G.A., 2015. MODIS/Terra Snow Cover Monthly L3 Global 0.05Deg CMG Dataset Version 6. https://nsidc.org/data/MOD10CM.

Hargreaves, G.H., Samani, Z.A., 1985. Reference crop evapotranspiration from temperature. Appl. Eng. Agric. 1, 96–99. https://doi.org/10.13031/2013.26773.

Harrison, S., Kargel, J.S., Huggel, C., Reynolds, J., Shugar, D.H., Betts, R.A., Emmer, A., Glasser, N., Haritashya, U.K., Klimeš, J., Reinhardt, L., Schaub, Y., Wiltshire, A., Regmi, D., Vilímek, V., 2018. Climate change and the global pattern of moraine-dammed glacial lake outburst floods. Cryosphere 12, 1195–1209. https://doi.org/10.5194/tc-12-1195-2018.

Hersbach, H., Bell, B., Berrisford, P., Hirahara, S., Horányi, A., Muñoz-Sabater, J., Nicolas, J., Peubey, C., Radu, R., Schepers, D., Simmons, A., Soci, C., Abdalla, S., Abellan, X., Balsamo, G., Bechtold, P., Biavati, G., Bidlot, J., Bonavita, M., De Chiara, G., Dahlgren, P., Dee, D., Diamantakis, M., Dragani, R., Flemming, J., Forbes, R., Fuentes, M., Geer, A., Haimberger, L., Healy, S., Hogan, R.J., Hólm, E., Janisková, M., Keeley, S., Laloyaux, P., Lopez, P., Lupu, C., Radnoti, G., de Rosnay, P., Rozum, I., Vamborg, F., Villaume, S., Thépaut, J.N., 2020. The ERA5 global reanalysis. Q. J. R. Meteorol. Soc. 146, 1999–2049. https://doi.org/10.1002/qj.3803.

Hock, R., 2003. Temperature index melt modelling in mountain areas. J. Hydrol. 282, 104–115. https://doi.org/10.1016/S0022-1694(03)00257-9.

Hock, R., 2005. Glacier melt: a review of processes and their modelling. Prog. Phys. Geogr. https://doi.org/10.1191/0309133305 pp453ra.

Hou, M., Cuo, L., Xu, H., 2025. Hydrological response to twenty-first century climate change in the Amu Darya Basin. Central Asia. J. Hydrol. Reg. Stud. 61, 102606. https://doi.org/10.1016/j.ejrh.2025.102606.

Huang, J., Barandun, M., Richard-Cerda, J., Hoelzle, M., Pohl, E., 2026. Winter baseflow calibration's critical role in hydrological modeling for the Pamir Region. Water Resour. Res. 62, e2025WR040043. https://doi.org/10.1029/2025WR040043.

Hugonnet, R., McNabb, R., Berthier, E., Menounos, B., Nuth, C., Girod, L., Farinotti, D., Huss, M., Dussaillant, I., Brun, F., Kääb, A., 2021. Accelerated global glacier mass loss in the early twenty-first century. Nat. 2021 5927856 592, 726–731. https://doi.org/10.1038/s41586-021-03436-z.

Huss, M., Hock, R., 2018. Global-scale hydrological response to future glacier mass loss. Nat. Clim. Chang. 1. https://doi.org/10.1038/s41558-017-0049-x.

Immerzeel, W.W., 2010. Climate change will effect the asian water tower. Science 1382. https://doi.org/10.1126/science.1183188.

Immerzeel, W.W., Wanders, N., Lutz, A.F., Shea, J.M., Bierkens, M.F.P., 2015. Reconciling high-altitude precipitation in the upper Indus basin 4673–4687. https://doi.org/10.5194/hess-19-4673-2015.
Immerzeel, W.W., Lutz, A.F., Andrade, M., Bahl, A., Biemans, H., Bolch, T., Hyde, S., Brumby, S., Davies, B.J., Elmore, A.C., Emmer, A., Feng, M., Fernández, A., Haritashya, U., Kargel, J.S., Koppes, M., Kraaijenbrink, P.D.A., Kulkarni, A.V., Mayewski, P.A., Nepal, S., Pacheco, P., Painter, T.H., Pellicciotti, F., Rajaram, H., Rupper, S., Sinisalo, A., Shrestha, A.B., Viviroli, D., Wada, Y., Xiao, C., Yao, T., Baillie, J.E.M., 2020. Importance and vulnerability of the world's water towers. Nature 577, 364–369. https://doi.org/10.1038/s41586-019-1822-y.
Ipcc, 2022. High Mountain areas. The Ocean and Cryosphere in a Changing Climate. https://doi.org/10.1017/9781009157964.010.
Jianqiao, H., Xiaodong, H., Xi, J., Wei, Z., 2025. Quantitative study of snow sublimation in the Altai Mountains. Atmos. Res. 321, 108109. https://doi.org/10.1016/j.atmosres.2025.108109.
Kalashnikova, O., Niyazov, J., Nurbatsina, A., Kodirov, S., Radchenko, Y., Kretova, Z., 2023. Kyrgyz transboundary rivers' runoff assessment (Syr-darya and Amu-darya river basins) in climate change scenarios. Cent. Asian J. Water Res. 9, 59–88. https://doi.org/10.29258/CAJWR/2023-R1.v9-1/59-88.eng.
Kang, S., Xu, Y., You, Q., Flügel, W.A., Pepin, N., Yao, T., 2010. Review of climate and cryospheric change in the Tibetan Plateau. Environ. Res. Lett. 5. https://doi.org/10.1088/1748-9326/5/1/015101.
Karimov, B.K., Shoergashova, S.S., Li, F., Talskikh, V.N., Latisheva, L.N., 2022. Chapter 21 - Impact of agricultural development on water quality in Zarafshan River, Uzbekistan, Central Asia: Trends since 1960s, in: Tiwari, A.K., Kumar, A., Singh, A. K., Singh, T.N., Suozzi, E., Matta, G., Russo, S.L. (Eds.), Water Scarcity, Contamination and Management. Elsevier, pp. 411–436. https://doi.org/https://doi.org/10.1016/B978-0-323-85378-1.00021-0.
Kayastha, R.B., Takeuchi, Y., Nakawo, M., Ageta, Y., 2000. Practical prediction of ice melting beneath various thickness of debris cover on Khumbu Glacier, Nepal, using a positive degree-day factor. Presented at the Debris-Covered Glaciers (Proceedings of a workshop held at Seattle, Washington, USA, September 2000), IAHS Publication, pp. 71–81.
Khaidarov, A., 2020. Water use in Uzbekistan's segment of the Zarafshan River: analytical review. Cent. Asian J. Water Res. 6, 89–105.
Khanal, S., 2021. Compound drivers of hydroclimatic extremes in large river basins: Mapping future floods and water resources by modeling compound drivers at multiple spatial and temporal scales.
Khanal, S., Lutz, A.F., Kraaijenbrink, P.D.A., van den Hurk, B., Yao, T., Immerzeel, W.W., 2021. Variable 21st century climate change response for Rivers in High Mountain Asia at seasonal to decadal time scales. Water Resour. Res. 57, e2020WR029266. https://doi.org/10.1029/2020wr029266.
Khanal, S., Tiwari, S., Lutz, A.F., Hurk, B.V.D., Immerzeel, W.W., 2023. Historical Climate Trends over High Mountain Asia Derived from ERA5 Reanalysis Data 263–288. https://doi.org/10.1175/JAMC-D-21-0045.1.
Kirches, G., Brockmann, C., Boettcher, M., Peters, M., Bontemps, S., Lamarche, C., Schlerf, M., Santoro, M., Defourny, P., 2014. Land cover cci-product user guide-version 2. ESA Public Doc. CCI-LC-PUG.
Kraaijenbrink, P.D.A., Bierkens, M.F.P., Lutz, A.F., Immerzeel, W.W., 2017. Impact of a global temperature rise of 1.5 degrees Celsius on Asia's glaciers. Nature 549, 257.
Lange, S., 2021. ISIMIP3b bias-adjusted atmospheric climate input data (v1.1). ISIMIP Repos.
Li, Z., Chen, Y., Li, Y., Wang, Y., 2020. Declining snowfall fraction in the alpine regions. Central Asia. Sci. Rep. 10, 3476. https://doi.org/10.1038/s41598-020-60303-z.
Lu, H., Jia, J., Yin, Q., Xia, D., Gao, F., Liu, H., Fan, Y., Li, Z., Wang, X., Berger, A., Oimuhammadzoda, I., Gadoev, M., 2020. Atmospheric dynamics patterns in Southern Central Asia since 800 ka revealed by loess-paleosol sequences in Tajikistan. Geophys. Res. Lett. 47, 1–10. https://doi.org/10.1029/2020GL088320.
Lutz, A.F., Immerzeel, W.W., Shrestha, A.B., Bierkens, M.F.P., 2014. Consistent increase in High Asia's runoff due to increasing glacier melt and precipitation. Nat. Clim. Chang. 4. https://doi.org/10.1038/nclimate2237.
Lyu, H., Fang, G., Chen, Y., Liang, W., Qiu, Z., Li, Y., Duan, W., Li, Z., 2026. Variations in glacier peak water timing and its influencing factors in High-Mountain Asia. Fundam. Res. 6, 324–334. https://doi.org/10.1016/j.fmre.2024.12.006.
Mandal, A., Angchuk, T., Azam, M.F., Ramanathan, A., Wagnon, P., Soheb, M., Singh, C., 2022. An 11-year record of wintertime snow-surface energy balance and sublimation at 4863 m a.s.l. on the Chhota Shigri Glacier moraine (western Himalaya, India). Cryosphere 16, 3775–3799. https://doi.org/10.5194/tc-16-3775-2022.
Mathys, T., Azimshoev, M., Bektursunov, Z., Hauck, C., Hilbich, C., Duishonakunov, M., Kayumov, A., Kassatkin, N., Kapitsa, V., Martin, L.C.P., Mollaret, C., Navruzshoev, H., Pohl, E., Saks, T., Silmonov, I., Musaev, T., Usubaliev, R., Hoelzle, M., 2025. Quantifying permafrost ground ice contents in the Tien Shan and Pamir (Central Asia): a petrophysical joint inversion approach using a geometric mean model. Cryosphere 19, 6591–6628. https://doi.org/10.5194/tc-19-6591-2025.
Menne, M.J., Durre, I., Vose, R.S., Gleason, B.E., Houston, T.G., 2012. An overview of the global historical climatology network-daily database. J. Atmos. Ocean. Technol. 29, 897–910. https://doi.org/10.1175/JTECH-D-11-00103.1.
Micklin, P., 2016. The future Aral Sea: hope and despair. Environ. Earth Sci. 75, 1–15. https://doi.org/10.1007/S12665-016-5614-5/METRICS.
Mihalcea, C., Mayer, C., Diolaiuti, G., Lambrecht, A., Smiraglia, C., Tartari, G., 2006. Ice ablation and meteorological conditions on the debris-covered area of Baltoro glacier, Karakoram, Pakistan. Ann. Glaciol. 43, 292–300. https://doi.org/10.3189/172756406781812104.
Miles, E., McCarthy, M., Dehecq, A., Kneib, M., Fugger, S., Pellicciotti, F., 2021. Health and sustainability of glaciers in High Mountain Asia. Nat. Commun. 12. https://doi.org/10.1038/s41467-021-23073-4.
Millan, R., Mouginot, J., Rabatel, A., Morlighem, M., 2022. Ice velocity and thickness of the world's glaciers. Nat. Geosci. 2022 152 15, 124–129. https://doi.org/10.1038/s41561-021-00885-z.
Mishra, S., 2009. Uncertainty and sensitivity analysis techniques for hydrologic modeling. J. Hydroinformatics 11, 282–296. https://doi.org/10.2166/HYDRO.2009.048.
Moriasi, D.N., Arnold, J.G., Liew, M.W.V., Bingner, R.L., Harmel, R.D., Veith, T.L., 2007. Model Evaluation Guidelines for Systematic Quantification of Accuracy in Watershed Simulations 50, 885–900.
Muhammad, S., Tian, L., Ali, S., Latif, Y., Wazir, M.A., Goheer, M.A., Saifullah, M., Hussain, I., Shiyin, L., 2020. Thin debris layers do not enhance melting of the Karakoram glaciers. Sci. Total Environ. 746, 141119. https://doi.org/10.1016/j.scitotenv.2020.141119.
Mukhamedjanov, S., Mukhomedjanov, A., Sagdullaev, R., Khasanova, N., 2021. Adaptation to climate change in irrigated agriculture in Uzbekistan. Irrig. Drain. 70, 169–176. https://doi.org/10.1002/ird.2529.
Murodov, A., Cuo, L., Li, N., Murodov, D., Hou, M., Hussain, G., 2023. Extreme hydrometeorological conditions and changes in the Amu Darya River Basin in Central Asia. J. Hydrometeorol. 24, 315–334. https://doi.org/10.1175/JHM-D-22-0025.1.
Murodov, M., Li, L., Weili, D., Nazrialo, S., Eshrat, F., Farhod, N., Khanal, S., Safarov, M., Murodov, A., Bu, L., Khusrav, K., Gulakhmadov, A., 2025. Impacts of future climate change on runoff and its components for the Vanj river basin in the western Pamir. J. Hydrol.: Reg. Stud. 62, 102916. https://doi.org/10.1016/j.ejrh.2025.102916.
Nash, J.E., Sutcliffe, J.V., 1970. River flow forecasting through conceptual models Part I-a discussion of principles*. J. Hydrol. 10, 282–290. https://doi.org/10.1016/0022-1694(70)90255-6.
Nzabarinda, V., Bao, A., Tie, L., Ochege, F.U., Uwamahoro, S., Kayiranga, A., Bao, J., Sindikubwabo, C., Li, T., 2024. The monsoon's influence on Central Asia's subsequent periods of drought and flooding. J. Geophys. Res. Atmos. 129, e2023JD040291. https://doi.org/10.1029/2023JD040291.
O'Hara, S.L., 2000. Central Asia's water resources: contemporary and future management issues. Int. J. Water Resour. Dev. 16, 423–441. https://doi.org/10.1080/713672501.
Obu, J., Westermann, S., Bartsch, A., Berdnikov, N., Christiansen, H.H., Dashtseren, A., Delaloye, R., Elberling, B., Etzelmüller, B., Kholodov, A., Khomutov, A., Kääb, A., Leibman, M.O., Lewkowicz, A.G., Panda, S.K., Romanovsky, V., Way, R.G., Westergaard-Nielsen, A., Wu, T., Yamkhin, J., Zou, D., 2019. Northern Hemisphere permafrost map based on TTOP modelling for 2000–2016 at 1 km2 scale. Earth Sci. Rev. 193, 299–316. https://doi.org/10.1016/J.EARSCIREV.2019.04.023.
Obu, J., Westermann, S., Vieira, G., Abramov, A., Ruby Balks, M., Bartsch, A., Hrbáček, F., Kääb, A., Ramos, M., 2020. Pan-Antarctic map of near-surface permafrost temperatures at 1 km2 scale. Cryosphere 14, 497–519. https://doi.org/10.5194/tc-14-497-2020.
Olsson, O., Gassmann, M., Wegerich, K., Bauer, M., 2010. Identification of the effective water availability from streamflows in the Zerafshan river basin, Central Asia. J. Hydrol. 390, 190–197. https://doi.org/10.1016/J.JHYDROL.2010.06.042.
Orsolini, Y., Wegmann, M., Dutra, E., Liu, B., Balsamo, G., Yang, K., Rosnay, P.D., Zhu, C., Wang, W., Senan, R., Arduini, G., 2019. Evaluation of snow depth and snow cover over the Tibetan Plateau in global reanalyses using in situ and satellite remote sensing observations 2221–2239.
Pahl-Wostl, C., 2007. Transitions towards adaptive management of water facing climate and global change. Water Resour. Manag. 21, 49–62. https://doi.org/10.1007/s11269-006-9040-4.
Pellicciotti, F., Buergi, C., Immerzeel, W.W., Konz, M., Shrestha, A.B., 2012. Challenges and uncertainties in hydrological modeling of remote hindu KushKarakoramHimalayan (HKH) Basins: suggestions for calibration strategies. Mt. Res. Dev. 32, 39–50. https://doi.org/10.1659/MRD-JOURNAL-D-11-00092.1.
Pellicciotti, F., Fontrodona-Bach, A., Rounce, D.R., Fyffe, C.L., Anderson, L.S., Ayala, Á., Brock, B.W., Buri, P., Fugger, S., Fujita, K., Gantayat, P., Groos, A.R., Immerzeel, W., Kneib, M., Mayer, C., MacDonell, S., McCarthy, M., McPhee, J., Miles, E., Purdie, H., Rets, E., Sakai, A., Shaw, T.E., Steiner, J., Wagnon, P., Winter-Billington, A., 2026. DCG-MIP: the debris-covered glacier melt model intercomparison experiment. Cryosphere 20, 1895–1928. https://doi.org/10.5194/tc-20-1895-2026.
Pena-Guerrero, M.D., Senay, G.B., Umirbekov, A., Tarasova, L., Rufin, P., Pulatov, B., Muller, D., 2026. Climate change has increased crop water consumption in Central Asia despite less water-intensive cropping. Commun. Earth Environ. 7, 122. https://doi.org/10.1038/s43247-025-03142-y.
Pepin, N., Bradley, R.S., Diaz, H.F., Baraër, M., Caceres, E.B., Forsythe, N., Fowler, H., Greenwood, G., Hashmi, M.Z., Liu, X.D., Others, 2015. Elevation-dependent warming in mountain regions of the world. Nat. Clim. Change 5, 424–430. https://doi.org/10.1038/nclimate2563.
Pohl, E., Gloaguen, R., Andermann, C., Knoche, M., 2017. Glacier melt buffers river runoff in the Pamir Mountains. Water Resour. Res. 53, 2467–2489. https://doi.org/10.1002/2016WR019431.
Pohl, E., Knoche, M., Gloaguen, R., Andermann, C., Krause, P., 2015. Sensitivity analysis and implications for surface processes from a hydrological modelling approach in the Gunt catchment, high Pamir Mountains. Earth Surf. Dyn. 3, 333–362. https://doi.org/10.5194/esurf-3-333-2015.
Qin, Y., Abatzoglou, J.T., Siebert, S., Huning, L.S., AghaKouchak, A., Mankin, J.S., Hong, C., Tong, D., Davis, S.J., Mueller, N.D., 2020. Agricultural risks from changing snowmelt. Nat. Clim. Chang. 10, 459–465. https://doi.org/10.1038/s41558-020-0746-8.

Ragettli, S., Kreiner, A., Yakovlev, A., Anarbekov, O., Al-Zu'bi, M., Urazkeldiyev, A., Siegfried, T., 2025. Unraveling agricultural water use in three Central Asian irrigation oases using remote sensing. J. Hydrol. Reg. Stud. 59, 102414. https://doi.org/10.1016/j.ejrh.2025.102414.

Reyer, C.P.O., Otto, I.M., Adams, S., Albrecht, T., Baarsch, F., Cartsburg, M., Coumou, D., Eden, A., Ludi, E., Marcus, R., Mengel, M., Mosello, B., Robinson, A., Schleussner, C. F., Serdeczny, O., Stagl, J., 2017. Climate change impacts in Central Asia and their implications for development. Reg. Environ. Chang. 17, 1639–1650. https://doi.org/10.1007/s10113-015-0893-z.

RGI Consortium, 2017. GLIMS: Global Land Ice Measurements from Space [WWW Document]. Dataset Glob. Glacier Outl. Version 60 Tech. Rep. Glob. Land Ice Meas. Space Colo. USA. https://doi.org/https://doi.org/10.7265/N5-RGI-60.

Rounce, D.R., Hock, R., Shean, D.E., 2020. Glacier mass change in High Mountain Asia through 2100 using the open-source python glacier evolution model (PyGEM). Front. Earth Sci. 7, 1–20. https://doi.org/10.3389/feart.2019.00331.

Sadyrov, S., Tanaka, K., Satylkanov, R., Khujanazarov, T., Touge, Y., Fujita, K., 2024. Modelling runoff components and hydrological processes in glaciated catchments of the inner Tien-Shan, Kyrgyzstan. Front. Earth Sci. 11. https://doi.org/10.3389/feart.2023.1306476.

Savoskul, O.S., Smakhtin, V.U., 2013. Glacier systems and seasonal snow cover in six major asian river basins: hydrological role under changing climate. International Water Management Institute. Doi 10 (5337/2013), 204.

Schaefli, B., Gupta, H.V., 2007. Do Nash values have value? Hydrol. Process. 21, 2075–2080. https://doi.org/10.1002/hyp.6825.

Siegfried, T., Bernauer, T., Guiennet, R., Sellars, S., Robertson, A.W., Mankin, J., Bauer-Gottwein, P., Yakovlev, A., 2012. Will climate change exacerbate water stress in Central Asia? Clim. Change 112, 881–899. https://doi.org/10.1007/s10584-011-0253-z.

Simons, G., Koster, R., Droogers, P., 2020. HiHydroSoil v2 . 0 - High Resolution Soil Maps of Global Hydraulic Properties 1–18.

Singh, P., Kumar, N., Arora, M., 2000. Degree-day factors for snow and ice for Dokriani Glacier, Garhwal Himalayas. J. Hydrol. 235, 1–11. https://doi.org/10.1016/S0022-1694(00)00249-3.

Sorg, A., Bolch, T., Stoffel, M., Solomina, O., Beniston, M., 2012. Climate change impacts on glaciers and runoff in Tien Shan (Central Asia). Nat. Clim. Change 2012 210 2, 725–731. https://doi.org/10.1038/nclimate1592.

Sorg, A., Huss, M., Rohrer, M., Stoffel, M., 2014. The days of plenty might soon be over in glacierized Central Asian catchments. Environ. Res. Lett. 9. https://doi.org/10.1088/1748-9326/9/10/104018.

Stigter, E.E., Litt, M., Steiner, J.F., Bonekamp, P.N.J., 2018. The Importance of Snow Sublimation on a Himalayan Glacier 6, 1–16. https://doi.org/10.3389/feart.2018.00108.

Sultonov, Z., Pant, H., 2026. Glacier Retreat in Tajikistan: A Looming Threat to Central Asia's Water Resources.

Terink, W., Lutz, A.F., Simons, G.W.H., Immerzeel, W.W., Droogers, P., 2015. SPHY v2. Spatial Processes in HYdrology 2009–2034. https://doi.org/10.5194/gmd-8-2009-2015.

UNEP, 2011. Environment and Security in the Amu Darya River Basin, 2011. Disasters 100.

Van Tricht, L., Huybrechts, P., Van Breedam, J., Vanhulle, A., Van Oost, K., Zekollari, H., 2021. Estimating surface mass balance patterns from unoccupied aerial vehicle measurements in the ablation area of the Morteratsch-Pers glacier complex (Switzerland). Cryosphere 15, 4445–4464. https://doi.org/10.5194/TC-15-4445-2021.

Veh, G., Korup, O., Walz, A., 2020. Hazard from Himalayan glacier lake outburst floods. PNAS 117, 907–912. https://doi.org/10.1073/pnas.1914898117.

Viviroli, D., Drenkhan, F., Scott, C.A., Somers, L., van Tiel, M., 2026. Cascading downstream impacts of water cycle changes in mountain regions. Nat. Clim. Chang. 16, 129–142. https://doi.org/10.1038/s41558-025-02552-2.

Westermann, S., Ostby, T.I., Gisnäs, K., Schuler, T., Etzelmüller, B., 2015. A ground temperature map of the North Atlantic permafrost region based on remote sensing and reanalysis data. Cryosphere 9, 1303–1319. https://doi.org/10.5194/TC-9-1303-2015.

Wijngaard, R.R., Lutz, A.F., Nepal, S., Khanal, S., Pradhananga, S., Shrestha, A.B., Immerzeel, W.W., 2017. Future changes in hydro-climatic extremes in the Upper Indus, Ganges, and Brahmaputra River basins. PLoS One 12, e0190224.

World Bank, 2024. Tajikistan General Water Security Assessment.

Xenarios, S., Gafurov, A., Schmidt-Vogt;, D., Sehring, J., Manandhar, S., Hergarten, C., Shigaeva, J., Foggin, M., 2019. Climate change and adaptation of mountain societies in Central Asia: uncertainties, knowledge gaps, and data constraints. Reg. Environ. Chang. 19, 1339–1352. https://doi.org/10.1007/s10113-018-1384-9.

Yan, X., Fang, G., Chen, Y., Li, Z., Cao, B., Gulakhmadov, A., Nasrulloev, F., Zhang, X., Liang, W., Lyu, H., Li, R., 2026. Study on the coupling processes of glaciers, snow and runoff in the Pamir Plateau. J. Hydrol.: Reg. Stud. 67, 103832. https://doi.org/10.1016/j.ejrh.2026.103832.

Yao, T., Bolch, T., Chen, D., Gao, J., Immerzeel, W., Piao, S., Su, F., Thompson, L., Wada, Y., Wang, L., Wang, T., Wu, G., Xu, B., Yang, W., Zhang, G., Zhao, P., 2022. The imbalance of the asian water tower. Nat. Rev. Earth Environ. 3, 618–632. https://doi.org/10.1038/s43017-022-00299-4.

Zhang, Q., Chen, Y., Li, Z., Fang, G., Xiang, Y., Sun, C., 2026. Glacier Change Threatens Central Asia's Water Towers. iScience 29, 114727. https://doi.org/10.1016/j.isci.2026.114727.

Zhu, M., Yao, T., Xie, Y., Xu, B., Yang, W., Yang, S., 2020. Mass balance of Muji Glacier, northeastern Pamir, and its controlling climate factors. J. Hydrol. 590, 125447. https://doi.org/10.1016/j.jhydrol.2020.125447.